Interacting Dirac fermions under a spatially alternating pseudomagnetic field: Realization of spontaneous quantum Hall effect

Citation: Venderbos, Jorn W. F., and Liang Fu. "Interacting Dirac Fermions Under a Spatially Alternating Pseudomagnetic Field: Realization of Spontaneous Quantum Hall Effect." Physical Review B 93, no. 19 (May 13, 2016). © 2016 American Physical Society

As Published: http://dx.doi.org/10.1103/PhysRevB.93.195126

Publisher: American Physical Society

Persistent URL: http://hdl.handle.net/1721.1/102656

Version: Final published version: final published article, as it appeared in a journal, conference proceedings, or other formally published context

Interacting Dirac fermions under a spatially alternating pseudomagnetic field: Realization of spontaneous quantum Hall effect

Jörn W. F. Venderbos and Liang Fu
Department of Physics, Massachusetts Institute of Technology, Cambridge, Massachusetts 02139, USA
(Received 24 June 2015; revised manuscript received 10 April 2016; published 13 May 2016)

Both topological crystalline insulator surfaces and graphene host multivalley massless Dirac fermions which are not pinned to a high-symmetry point of the Brillouin zone. Strain couples to the low-energy electrons as a time-reversal-invariant gauge field, leading to the formation of pseudo-Landau-levels (PLLs). Here we study periodic pseudomagnetic fields originating from strain superlattices. We study the low-energy Dirac PLL spectrum induced by the strain superlattice and analyze the effect of various polarized states. Through self-consistent Hartree-Fock calculations we establish that, due to the strain superlattice and PLL electronic structure, a valley-ordered state spontaneously breaking time reversal and realizing a quantum Hall phase is favored, while others are suppressed. Our analysis applies to both topological crystalline insulators and graphene.

DOI: 10.1103/PhysRevB.93.195126

I. INTRODUCTION

The discovery of graphene and topological insulators has significantly boosted the ubiquity of condensed matter realizations of Dirac fermions as emergent electronic excitations at low energy [1–3]. Dirac electrons in condensed matter systems have enjoyed an enormous amount of interest from both a fundamental and a technological application perspective [4]. A key difference between graphene and topological insulators is the number of species, or valleys, of Dirac fermions and their locations in momentum space. Topological insulators (TIs) protected by time reversal symmetry host a single-valley Dirac fermion, which is pinned to a time-reversal-invariant (TRI) momentum in the surface Brillouin zone [5]. In contrast, graphene hosts two valleys of Dirac fermions located at non-TRI momenta [6,7], each valley having an additional spin degeneracy. More recently, a new type of Dirac fermions was discovered on the surface of topological crystalline insulators (TCIs) SnTe, (Sn,Pb)Se, and (Sn,Pb)Te [8–13], which are protected by mirror symmetry of the crystal [8,14–16]. These Dirac fermions exhibit spin-momentum locking as in TIs; however, there is an even number of Dirac cones at non-TRI momenta, a feature similar to graphene.

In general, when Dirac points are located at non-TRI momenta, nonmagnetic perturbations such as strain are able to move Dirac points in momentum space, thereby acting as an effective gauge field on Dirac fermions. For example, strain induces opposite gauge fields for the two Dirac valleys in graphene, and spatially inhomogeneous strain gives rise to effective magnetic fields that are opposite in two valleys, preserving time reversal symmetry [17–19]. In the presence of such a pseudomagnetic field $\mathcal{B}$, the low-energy electronic structure takes the form of pseudo-Landau-levels (PLLs) with energies characteristic of Dirac electrons in magnetic fields, i.e., $\sim\sqrt{n\mathcal{B}}$, where n is the Landau level (LL) index. Key signatures of pseudomagnetic fields have been experimentally observed in graphene [20,21].

The PLLs have a large single-particle degeneracy, which makes them susceptible to many-body instabilities in a manner similar to magnetic-field-induced LLs [22]. Electronic interactions are expected to lift the degeneracy and drive the system into various gapped states. Two primary examples are spin-polarized and valley-polarized states of PLLs in graphene [23–28].

In this work we consider interacting Dirac electrons under *periodically* modulated pseudomagnetic fields, where regions of positive and negative fields alternate in space, forming a superlattice. This field profile leads to an electronic structure markedly different from uniform pseudomagnetic fields [29,30]. There are various ways in which periodic pseudomagnetic fields can arise, one prominent way being a strain superlattice in graphene or TCIs. Such spatially periodic strain fields are particularly relevant, as they were experimentally found to develop at interfaces of heterostructures built from TCIs (e.g., SnTe) and trivial insulators (e.g., PbTe) [31–33]. At these interfaces, the lattice constant mismatch causes dislocations which self-organize into a periodic array and therefore produce a natural realization of periodic strain fields. The key characteristic of the corresponding periodic pseudomagnetic fields is that they can exist over macroscopic regions. In contrast, uniform pseudomagnetic fields cannot exist in the thermodynamic limit, owing to the boundedness of strain (=pseudogauge field) [30], unlike a real magnetic field. Apart from strain superlattices, periodic pseudomagnetic fields can arise as a result of incommensurate electrostatic potentials originating, for instance, from lattice-mismatched substrates with a twist angle [34–36].

Starting from the strain-induced pseudomagnetic superlattice, we address the effect of electron-electron interactions. Spatially alternating pseudomagnetic fields change the low-energy electronic structure close to the Dirac points. Most strikingly, the energy-momentum dispersion in the vicinity of *each* Dirac point becomes nearly flat, leading to a segment of flat band with a *twofold* degeneracy. These flat bands arise from the zeroth PLL in regions with strong pseudomagnetic fields; and the twofold degeneracy corresponds to Landau orbitals that reside in different spatial regions of opposite fields and have opposite Dirac spinor components [30], a feature that is absent in the case of uniform magnetic fields. Counting the two valleys, the flat bands have fourfold degeneracy. The presence of flat bands leads to a diverging density of states, in contrast to the vanishing density of states at the Dirac point of massless Dirac fermions. Consequently, periodic strain fields provide a feasible and effective way of engineering

density of states, i.e., electronic compressibility, at zero energy.

At charge neutrality, the degenerate flat bands are mainly responsible for driving the spontaneous formation of ordered states. We discuss the various possibilities for degeneracy lifting in the flat band and discriminate between energetically favorable and unfavorable states. Two prominent candidate ordered states are the charge-ordered state, where charge is redistributed from the region of positive (negative) to negative (positive) pseudomagnetic field, and the valley-ordered state, where in each spatial region the valley degeneracy is lifted. We show that the valley-ordered state in graphene and TCIs spontaneously breaks time reversal symmetry and realizes an integer quantum Hall effect similar to the Haldane state [7], but with the important difference of being driven by electron interactions without any external time-reversal-breaking field.

We determine the mean-field ground state by self-consistently solving the full gap equation of interacting Dirac fermions under a periodically alternating pseudomagnetic field. The continuum Hamiltonian is microscopically implemented using a lattice model with a strain superlattice. Our analysis shows that the support of the flat band wave functions is of great importance. Flat bands in any spatial region only have a twofold valley degeneracy, protected by the time reversal symmetry. Therefore lifting this degeneracy by interactions implies time reversal symmetry breaking. For this reason, we find the valley-ordered quantum Hall state is greatly favored over the charged-ordered state under generic forms of electron interactions. We show that the order parameters corresponding to the ordered states follow the strain profile, highlighting the crucial role of the pseudomagnetic field.

The present setup for a spontaneous time-reversal-symmetry-breaking quantum Hall state relying on a strain-induced flat band should be contrasted with the proposed Haldane mass generation for interacting massless Dirac fermions in graphene [37–39]. Exact diagonalization and DMRG studies [40–44] seem to have failed to find the interaction-driven Haldane phase in models so far proposed, in contradiction to Hartree-Fock results. It is believed that the absence of the Haldane phase in ED and DMRG phase diagrams stems from the vanishing density of states at the Dirac point, and the resulting absence of a weak-coupling instability. In contrast, the quantum Hall state in our setup already occurs spontaneously at weak coupling, owing to the strain-induced flat band. Our setup may be compared to proposals for manipulating graphene bands through chirally stacking graphene layers [45].

II. DIRAC FERMIONS IN TWO DIMENSIONS

We set out to study the coupling of time-reversal-invariant pseudogauge fields to Dirac electrons. With two specific realizations in mind (i.e., graphene and TCI surface states) we focus on Dirac electrons in two dimensions (2D). We start by stating the essential features of Dirac electrons coupled to pseudogauge fields, which are independent of specific context.

A 2D system respecting time reversal invariance and with Dirac fermions not pinned to a particular time-reversal-invariant momentum will consist of (at least) two species of Dirac fermions. Labeling the two species by $+$ and $-$, the Dirac Hamiltonian describing the two species takes the general form

$$\hat{\mathcal{H}}_\pm = \pm\hbar v_F \hat{\Psi}_\pm^\dagger(-i\tau^x\partial_x - i\tau^y\partial_y)\hat{\Psi}_\pm, \tag{1}$$

where τ^i is a set of Pauli matrices acting on the pseudospin degree of freedom of the Dirac fermions. Time reversal symmetry relates the two species by exchanging $\hat{\Psi}_+ \leftrightarrow \hat{\Psi}_-$.

Pseudogauge fields couple to the Dirac fermions in a manner similar to real electromagnetic gauge fields, with one crucial difference, however. In order to respect time reversal invariance, the pseudogauge field must couple to the fermions in such a way that the two species see opposite fields. As a result, in the presence of a pseudogauge field given by $\mathcal{A}_\mu$ (where $\mu = x, y$), the Dirac Hamiltonian becomes

$$\hat{\mathcal{H}}_\pm = \pm v_F \hat{\Psi}_\pm^\dagger \tau^\mu(-i\partial_\mu \pm \mathcal{A}_\mu)\hat{\Psi}_\pm. \tag{2}$$

This Hamiltonian captures the essential features of Dirac electrons coupled to pseudogauge fields. Pseudo-Landau-level quantization will occur when the gauge field $\mathcal{A}_\mu$ acquires spatial dependence, i.e., when $\mathcal{A}_\mu = \mathcal{A}_\mu(\vec{r})$.

The interpretation of the Dirac fermion pseudospin and valley degree of freedom ($\pm$) will depend on the particular realization of pseudomagnetic field coupling in a given material. In this work, we will discuss two examples of low-energy Dirac electrons coupled to time-reversal-invariant gauge fields: we consider the case of graphene and that of surface states of TCIs. Whereas in graphene the Dirac pseudospin degree of freedom derives from the two sublattices [6], the pseudospin of the TCI surface state is more complicated due to intrinsic spin-orbit coupling, as we will discuss below. Importantly, in the case of the latter, spin-orbit coupling leads to spin-momentum locking in the surface state Dirac theory.

In both cases, graphene and TCIs, the emphasis will be on strain-induced pseudomagnetic field coupling. However, we will use the case of graphene to point out that pseudomagnetic fields can have a physical origin different from strain, giving way to an even wider application of our results.

A. Dirac fermions in graphene

The low-energy theory of graphene at charge neutrality is one of the hallmark examples of a 2D Dirac theory [4,6,46]. The two species of nodal Dirac fermions are located at the two inequivalent BZ corners (i.e., the Dirac points or valleys) and are labeled by K_+ and K_- corresponding to the momenta $\vec{K}_+ = (4\pi/3, 0)$ and $\vec{K}_- = -(4\pi/3, 0)$. The Dirac Hamiltonian is obtained by expanding the band structure around $K_\pm$ in small momenta $\vec{q}$ relative to $K_\pm$ [6]. It is given by

$$\mathcal{H}(\vec{q}) = \hbar v_F \nu^z(q_x\tau^x + q_y\tau^y) \equiv \hbar v_F q_\mu \Gamma_\mu \tag{3}$$

[where $v_F = \sqrt{3}ta/(2\hbar)$]. The set of Pauli matrices τ^i acts on the sublattice degree of freedom (A/B) and the set of matrices ν^i acts on the valley degree of freedom (K_+/K_-). In addition, we have defined the Dirac matrices $\Gamma_x = \nu^z\tau^x$ and $\Gamma_y = \nu^z\tau^y$. The Hamiltonian acts on the Dirac spinor $\hat{\Psi}(\vec{q}) = (\hat{\psi}_{A+}(\vec{q}), \hat{\psi}_{B+}(\vec{q}), \hat{\psi}_{B-}(\vec{q}), \hat{\psi}_{A-}(\vec{q}))^T$. Note that we have chosen a basis for which A and B are exchanged in the K_- valley (i.e., the chiral representation).

Starting from the low-energy Dirac Hamiltonian of Eq. (3), we introduce a generalized time-reversal-invariant

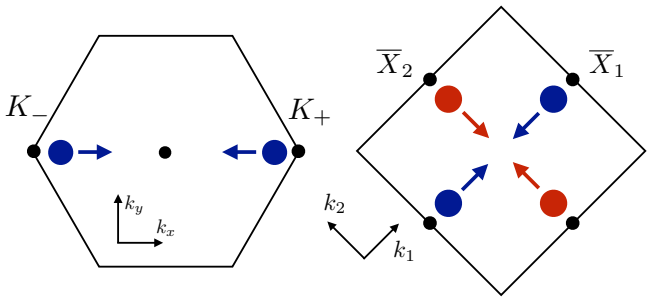

FIG. 1. Left: Hexagonal Brillouin zone of the honeycomb lattice. The two Dirac points K and K are marked by bold blue dots. The blue arrows indicate possible Dirac points moving towards the zone center due to strain, i.e., $\sim u_{xx} - u_{yy}$. Right: Square surface Brillouin of TCI surface state with two sets of Dirac points located at $\overline{X}_1$ (blue) and $\overline{X}_2$ (red). Arrows indicate the moving of Dirac points towards the zone center due to symmetric strain $\sim u_{xx} + u_{yy}$.

pseudogauge field by coupling the Dirac fermions to the field

$$\vec{\mathcal{A}}^i = \left(\mathcal{A}^i_x, \mathcal{A}^i_y\right), \tag{4}$$

which consists of three components $i = 1,2,3$. The coupling to the fermions has the same form as ordinary minimal coupling, but with different gauge charges Ω^i expressed as

$$\mathcal{H}(\vec{q}) = \hbar v_F \Gamma_\mu \left(q_\mu + \mathcal{A}^i_\mu \Omega^i\right). \tag{5}$$

The gauge charge matrices Ω^i encode the distinct nature of the pseudogauge field components as compared to the ordinary electromagnetic gauge field, and are given by $\Omega^i = (\nu^x\tau^z, \nu^y\tau^z, \nu^z)$. The third gauge charge matrix $\Omega^3 = \nu^z$ is diagonal in valley space and assigns opposite sign to the two valleys. Therefore, the component $\mathcal{A}^3_\mu \Omega^3$ realizes the general Hamiltonian of Eq. (2) in graphene. In graphene, this is the pseudogauge field component which arises in the presence of strain, and plays a central role in this work. The presence of a pseudogauge field $\vec{\mathcal{A}}^3$ coupling to Ω^3 leads to a moving of the Dirac points away from K_+ and K_-, in opposite directions. This is shown in Fig. 1 (left), where the bold blue dots denote the Dirac points moving towards the zone center.

The following properties of the gauge field charges will be important for our analysis. The charges Ω^i realize a pseudospin SU(2) algebra, expressed as $[\Omega^i, \Omega^j] = 2i\epsilon^{ijk}\Omega^k$. The matrices Ω^i commute with the Hamiltonian in the absence of fields, and as a consequence generate a continuous SU(2) symmetry of the low-energy graphene Hamiltonian. This symmetry is broken when mass terms are introduced to the Hamiltonian, i.e., when the Dirac electrons are gapped out. In particular, the set of mass matrices $\vec{\Gamma} = (\Gamma_1, \Gamma_2, \Gamma_3) \equiv (\nu^x, \nu^y, \nu^z\tau^z)$ describes masses which anticommute both with the Hamiltonian and between themselves. They constitute a set of compatible masses, the physical nature of which is well known. Specifically, the mass $\Gamma_3 = \nu^z\tau^z$ corresponds to an electrostatic potential making the two honeycomb sublattices inequivalent and breaking inversion symmetry. Such term is diagonal in valley space; i.e., it does not couple the two Dirac points. The other two masses, Γ_1 and Γ_2, which are off-diagonal in valley space, are known as Kekulé masses and correspond to modulations of the tight-binding nearest-neighbor-hopping parameter t with tripled unit cell [47]. The breaking of translational invariance and the modulations over small distances (large momenta) couple the Dirac points.

The gauge charges Ω^i act as generators of rotations within the space of masses, which follows from the commutation relation $[\Omega^i, \Gamma_j] = 2i\epsilon^{ijk}\Gamma_k$. In addition to the mass terms $\vec{\Gamma}$, there is a mass term τ^z, the time-reversal-odd Haldane mass [7], which anticommutes with the Hamiltonian (3), but commutes with both the Γ_i and the Ω^i. Hence, whereas $\vec{\Gamma}$ is a vector under the transformations generated by Ω^i, τ^z is a scalar.

The two remaining gauge charges $\Omega^1 = \nu^x\tau^z$ and $\Omega^2 = \nu^x\tau^z$ are off-diagonal in valley space but diagonal in sublattice space. The former implies translational symmetry breaking and the latter implies that these terms arise due to charge density modulations. Consequently, charge density waves (CDWs) with a six-site unit cell, which we will refer to as valley-coupling CDWs, lead to a pseudogauge coupling in the same way as strain [34]. The SU(2) structure of the gauge charges Ω^i implies that within the low-energy theory, the pseudogauge field components are unitarily equivalent to each other.

B. TCI surface state Dirac fermions

Topological insulator materials are bulk insulators hosting gapless Dirac fermions at their surfaces [1,2]. The spin-momentum-locked surface Dirac fermions are protected by time reversal symmetry, and as a result they are pinned at the time-reversal-invariant momenta (TRIM). Due to this symmetry-protected pinning, the surface states of topological insulators do not allow for time-reversal-invariant pseudogauge field coupling. In particular, strain is not able to move the Kramers doublet away from the TRIM.

In contrast, the TCIs are topological materials protected by crystalline symmetries [8,13], which host surface Dirac fermions not pinned to the TRIM [16,48,49]. As a result, strain can couple to the low-energy Dirac fermions as a pseudogauge field and can move the Dirac points in momentum space, in a way that depends on the symmetry of the strain tensor [16,30].

In this work we specifically focus on the SnTe material class [8] and its mirror-symmetry-protected surface Dirac fermions appearing on the (001) surface. The surface Brillouin zone of the (001) surface is shown in Fig. 1. Two species of low-energy Dirac fermions related by time reversal symmetry exist in the vicinity of the surface time-reversal-invariant momenta $\overline{X}_1$ and $\overline{X}_2$, represented as blue and red dots in Fig. 1. The surface state Dirac Hamiltonian at $\overline{X}_1$, given by the terms that respect the crystal symmetries leaving $\overline{X}_1$ invariant, reads

$$\mathcal{H}_{\overline{X}_1}(\vec{q}) = v_1 q_1 \sigma^y - v_2 q_2 \sigma^x + m\nu^x + \delta\sigma^x\nu^y, \tag{6}$$

and a similar expression can be derived for $\overline{X}_2$. Here σ^i is a set of Pauli matrices that represents a Kramers doublet, and ν^i is a valley degree of freedom corresponding to the two inequivalent bulk L points mapped onto $\overline{X}_1$. The momentum $\vec{q}$ is measured with respect to $\overline{X}_1$; the spin-momentum locking shown in Hamiltonian (6) (i.e., first two terms) comes from spin-orbit coupling. For $m = \delta = 0$ there are two degenerate Kramers doublets at $\overline{X}_1$, which are split in energy by finite m

and δ. Most importantly, finite m and δ lead to the appearance of two species of low-energy Dirac points, which are located at $\vec{\Lambda}_\pm = (0, \pm\sqrt{m^2+\delta^2}/v_2)$, measured from $\overline{X}_1$.

The Hamiltonian of Eq. (7) can be projected into the subspace corresponding to $\vec{\Lambda}_\pm$ to obtain the effective low-energy Dirac theory. This yields [16]

$$\mathcal{H}_{\vec{\Lambda}_\pm}(\vec{q}) = -v_1' q_1 \tilde{\tau}^x + v_2 q_2 \tilde{\tau}^z, \tag{7}$$

where $\tilde{\tau}^i$ is the effective pseudospin degree of freedom, $\vec{q}$ is now measured with respect to $\vec{\Lambda}_\pm$, and $v_1' = v_1\delta/\sqrt{m^2+\delta^2}$. Note that in the chosen basis the Hamiltonian is valley-isotropic, taking $\tilde{\nu}^z = \pm 1$ as an effective valley degree of freedom.

With the Hamiltonian of Eq. (7) we have arrived at a description of the low-energy Dirac fermions that has the general form introduced in the beginning of this section, and is thus similar to the graphene Hamiltonian of Eq. (3). Hence, in a way analogous to graphene, we can use symmetry arguments to establish the effect of various perturbations. For instance, since the TCI surface states are protected by mirror symmetry, one expects mirror symmetry breaking to open up a gap. We find two such gap opening mass terms, which do not couple the low-energy valleys, and they are given in the basis of (7) as $\tilde{\tau}^z$ and $\tilde{\nu}^z\tilde{\tau}^z$. The former is a time-reversal-even mass and corresponds to a ferroelectric distortion of the crystal. It derives from the Dirac bilinear ν^z in the basis of (6). The mass term $\tilde{\nu}^z\tilde{\tau}^z$ breaks time reversal symmetry and originates from the terms σ^z and $\sigma^y\nu^z$ in the basis of Eq. (6). The mass gap originating from $\tilde{\nu}^z\tilde{\tau}^z$ is equivalent to the graphene Haldane gap, and consequently corresponds to a QAH phase [16].

Similarly, by using symmetry arguments, the time-reversal-invariant pseudogauge field couplings can be identified. As a consequence of the low symmetry of the $\overline{X}_1$ point, there are no two-dimensional representations which directly imply pseudogauge coupling. However, since the symmetric terms ν^x and $\sigma^x\nu^y$ displace the Dirac points in momentum space, any perturbation coupling to them will have the effect of a pseudogauge field. Looking for other terms both even under time reversal and inversion (as expected for strain), one finds another Dirac bilinear given by $\sigma^y\nu^y$. We will show in the next section, when we discuss strain and strain superlattices, that components of the strain tensor couple to these terms. The effect of these terms is shown schematically in Fig. 1 (right), where bold blue and red dots denote the Dirac points in the vicinity of $\overline{X}_1$ and $\overline{X}_2$, respectively, shifting towards the zone center as a result of strain.

III. PERIODIC STRAIN SUPERLATTICES

In the previous section we introduced pseudogauge field coupling in the context of graphene and TCI surface states. Strain is a natural realization of such coupling. We now turn to a more detailed discussion of strain, in particular *periodic* pseudomagnetic fields arising due to periodically varying strain: a strain superlattice.

Elastic deformations of the crystal lattice are described by the strain tensor u_{ij} given by $u_{ij} = (\partial_i u_j + \partial_j u_i)/2$, where u_i $(i = x,y)$ is the displacement field. Given the symmetry of the crystal lattice, the strain tensor can be decomposed into components transforming as distinct representations of the symmetry group. From this decomposition one can read off which lattice deformations couple as (pseudo)gauge fields to the Dirac fermions.

Graphene has hexagonal symmetry and this implies two d-wave strain components $(u_{xx}-u_{yy}, -2u_{xy}) \sim (d_{x^2-y^2}, d_{xy})$ which couple to the Dirac fermions as the valley-diagonal field $\vec{\mathcal{A}}^3$ of Eq. (5) [50]. We thus have (we omit the label 3, i.e., $\vec{\mathcal{A}} = \vec{\mathcal{A}}^3$, for the moment)

$$\begin{pmatrix}\mathcal{A}_x\\ \mathcal{A}_y\end{pmatrix} \sim \alpha\begin{pmatrix}u_{xx}-u_{yy}\\ -2u_{xy}\end{pmatrix}, \tag{8}$$

with a single coupling constant α due to the degeneracy of the d waves. For illustration purposes, the effect of finite and constant $\mathcal{A}_x$ is shown graphically in Fig. 1 (left), where the Dirac points K_+ and K_- move along the k_x axis. In the case of the square symmetry, which applies to the (001) surface states of TCIs, the d-wave components $d_{x_1^2-x_2^2}$ and $d_{x_1x_2}$ are not degenerate, and one finds at $\overline{X}_1$ [30]

$$\begin{pmatrix}\mathcal{A}_x\\ \mathcal{A}_y\end{pmatrix} \sim \begin{pmatrix}\alpha_1(u_{xx}-u_{yy})\\ \alpha_2 u_{xy}\end{pmatrix}, \tag{9}$$

with coupling constants $\alpha_{1,2}$. In addition, in the previous section we observed that a perturbation respecting all symmetries can move the Dirac points in momentum space, implying that $u_{xx}+u_{yy}$ enters the expression for $\mathcal{A}_x$ as well, with an independent coupling. It is the latter strain component, $u_{xx}+u_{yy}$, the effect of which is shown in Fig. 1 (right).

We now come to the case of periodic strain fields with wavelength λ. More specifically, we consider $u_{ij} \to u_{ij}(\vec{r})$ which implies $\vec{\mathcal{A}} \to \vec{\mathcal{A}}(\vec{r})$. The periodicity of $\vec{\mathcal{A}}(\vec{r})$ is directly reflected in the periodicity of the pseudomagnetic field $\mathcal{B}(\vec{r}) = \vec{\nabla}\times\vec{\mathcal{A}}(\vec{r})$, which should be compared to and contrasted with a uniform pseudomagnetic field $\mathcal{B}$. In order to implement the strain superlattice in a tight-binding setting, we take the graphene lattice as a simple regularization of the continuum theory. To solve the superlattice Hamiltonian, we establish a connection between the strain components and the change in overlap integrals δt_n, where $n = 1,2,3$ labels the three nearest-neighbor vectors $\{\vec{\delta}_n\}$. The overlap integral change is expressed in terms of the strain tensor u_{ij} as $\delta t_n = \sum_n \delta_n^i \delta_n^j u_{ij}$, which becomes

$$\begin{pmatrix}u_{xx}-u_{yy}\\ -2u_{xy}\end{pmatrix} \sim \begin{pmatrix}2\delta t_1 - \delta t_2 - \delta t_3\\ \sqrt{3}(\delta t_2 - \delta t_3)\end{pmatrix}. \tag{10}$$

This expresses the pseudogauge field in terms of the modulation of the hopping $t_n \to t + \delta t_n$.

We proceed to consider a single-propagation vector pseudogauge field modulation and obtain the electronic spectrum. A particularly convenient choice is the propagation vector $\delta\vec{G} \equiv \vec{G}/\lambda$, where $\vec{G} = (0, 4\pi/\sqrt{3})$ is a reciprocal lattice vector. Then λ is the superlattice wavelength, given in terms of graphene unit cells; e.g., $\lambda = 700$ leads to a superlattice unit cell containing 700 graphene unit cells. The pseudogauge field

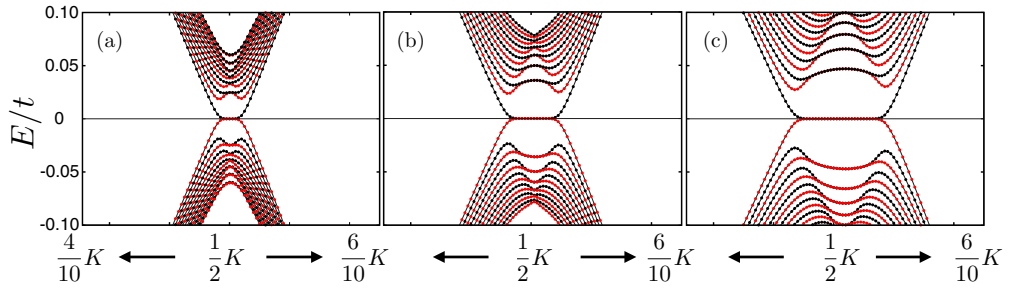

FIG. 2. Spectra of graphene in the presence of periodically modulated strain for different values of the amplitude of modulation (given by $A \sim 2\delta t_1 - \delta t_2 - \delta t_3$; see main text). The modulation wavelength λ is chosen to be 700 graphene unit cells and the propagation vector is $\delta\vec{G} = (0, 4\pi/\sqrt{3})/\lambda$. The amplitudes are (a) $A = 0.01t$, (b) $A = 0.03t$, (c) $A = 0.05t$. Note that the plots show K' folded onto the k_x axis.

$\vec{\mathcal{A}}$ and corresponding pseudomagnetic field are given by

$$\mathcal{A}_x(\vec{r}) = A\cos(\delta\vec{G}\cdot\vec{r}),$$
$$\mathcal{B}(\vec{r}) = -\partial_y\mathcal{A}_x = \delta G_y A\sin(\delta\vec{G}\cdot\vec{r}), \tag{11}$$

while $\mathcal{A}_y = 0$, since we are only interested in the transverse component. Here, A denotes the amplitude of the strain field, i.e., the maximal change in overlap δt.

The spectra in the presence of the strain superlattice for a number of values of A are shown in Fig. 2. We observe that upon increasing A, implying increasing pseudomagnetic field strength, a flat zero-energy band forms at the Dirac points, in addition to higher energy dispersive but doubly degenerate bands. This specific reorganization of the low-energy electronic spectrum resembles the Landau level structure of external magnetic fields. We will establish a detailed connection between Landau level physics and periodic strain in the next section. A key feature we wish to stress here is that the formation of the zero-energy flat band, the degeneracy of which is related to the strength of the pseudomagnetic field, leads to a finite and considerable density of states (DOS) at the charge neutrality point. In stark contrast, in the unstrained case Dirac electrons have linearly vanishing DOS at the charge neutrality point.

Instead of the propagation vector $\delta\vec{G}$, we can take the propagation vector as $\delta\vec{K} = \vec{K}/\lambda$, where $\vec{K}$ is the Dirac point vector defined in Sec. II A. This may be viewed as a simple rotation of $\delta\vec{G}$, which will result in a modified Moiré pattern of bond modulations. We then have for the spatially dependent pseudogauge field

$$\mathcal{A}_x(\vec{r}) = A\cos(\delta\vec{K}\cdot\vec{r}),$$
$$\mathcal{B}(\vec{r}) = -\partial_y\mathcal{A}_x = \delta K_y A\sin(\delta\vec{K}\cdot\vec{r}), \tag{12}$$

where is it important to choose $\vec{K}$ such that the field has a nonzero transverse component. For given λ, the strain superlattice unit cell contains 3λ graphene unit cells, which has the benefit that it is commensurate with any perturbation modulated by $\vec{K}$ coupling the Dirac points. This choice of strain superlattice has the benefit of allowing us to treat valley-diagonal and valley-off-diagonal perturbations on the same footing.

At this stage, we recall that the low-energy Dirac Hamiltonian in the presence of strain reads $\mathcal{H} = \hbar v_F\Gamma_\mu[-i\partial_\mu + \mathcal{A}^3_\mu(\vec{r})\Omega^3]$ (where we reinstated that label 3). As discussed in Sec. II A, a unitary matrix U can be used to rotate to another gauge field component, $U^\dagger\mathcal{H}U = \hbar v_F\Gamma_\mu(-i\partial_\mu + \mathcal{A}^1_\mu(\vec{r})\Omega^1)$. Clearly, this does not change the spectrum and therefore electrostatic potential superlattices, which would couple to the gauge field components Ω^1 and Ω^2 [36], are equivalent to strain superlattices. As a result, even though we focus on strain in this work, we highlight that in the context of graphene spatially modulated valley-coupling CDWs induce periodic time-reversal-invariant pseudomagnetic fields in the same way as strain.

IV. FLAT BAND PSEUDO-LANDAU-LEVELS INDUCED BY STRAIN

In this section we address the spectral properties of Dirac electrons in the presence of a time-reversal-invariant pseudomagnetic field. As in the previous section, we particularize to the case of graphene (i.e., our lattice regularization of the continuum theory), and start by briefly recalling the physics of a spatially uniform field induced by strain. Uniform fields are fundamentally different from periodically modulated fields induced by the strain superlattice, but we can use the results for the former to develop an intuition for the case of periodic pseudomagnetic fields. In particular, we may, for the sake of argument, think of the periodic field as alternating regions of positive and negative constant fields, which is schematically shown in Fig. 3 (top).

A. Uniform pseudomagnetic fields and PLLs

We start from the Hamiltonian of Eq. (4) and only retain the strain component $\vec{\mathcal{A}} \equiv \vec{\mathcal{A}}^3$,

$$\mathcal{H}(\vec{q}) = \hbar v_F\Gamma_x(q_x + \mathcal{A}_x\Omega^3) + \hbar v_F\Gamma_y(q_y + \mathcal{A}_y\Omega^3), \tag{13}$$

and $\vec{\mathcal{A}}(\vec{r})$ is taken so as to describe a constant field $\mathcal{B}$. The mathematical structure of the Hamiltonian is equivalent to that of a (time-reversal-breaking) magnetic field, and the standard techniques can be employed to solve it (see Appendix A). In particular, due to the formal equivalence, the energy spectrum is the same. Labeling the PLLs by n, the Landau level energies are given by $E_\pm(n) = \pm\sqrt{2\xi^2 n}$ $(n \geqslant 1)$ for each valley. Here we have defined $\xi^2 = v_F^2\hbar^2/l_b^2$. In addition to these finite energy states, the PLL spectrum contains zero energy states, the $E = 0$ zero modes.

Whereas the energies of PLLs are the same as those of magnetic field Landau levels, the structure of the eigenstates

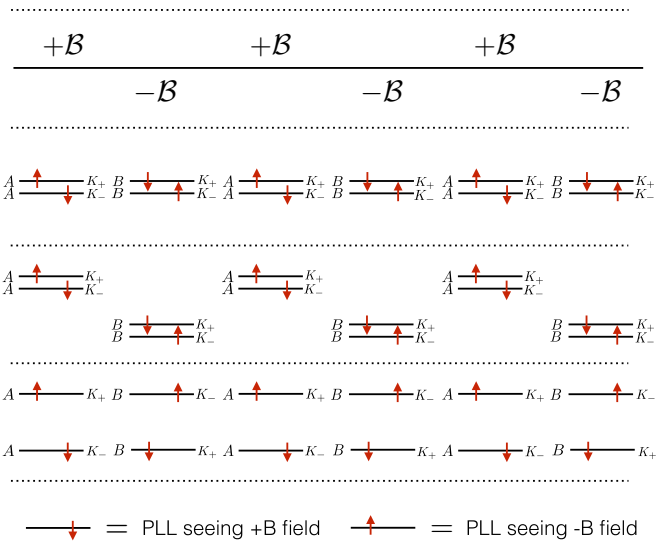

FIG. 3. Schematic representation of the PLL structure in the case of spatially alternating pseudomagnetic field. The alternating regions of positive and negative field are depicted in the upper row. In the row below we depict the degenerate $n = 0$ PLLs in the two regions, the structure of which periodically alternates in accordance with the field: in the $+\mathcal{B}$ ($-\mathcal{B}$) region, the PLLs are localized on the A (B) Dirac pseudospin degree of freedom and K_+ (K_-) valley sees a $+\mathcal{B}$ ($-\mathcal{B}$) field. Here A and B label a general pseudospin degree of freedom, which corresponds to the A/B sublattice in graphene. The bottom two rows show the two prime candidates for polarized states. In the charge-ordered state with ferroelectric polarization, the energy levels in the positive field (A) have higher energy than the negative field (B) states, the latter being fully occupied. In the valley-ordered quantum Hall state or anti-ferro-valley polarized state (very bottom) levels are split in each region, occupying a single valley in each region.

is different. We illustrate this by considering the eigenstates of the PLL zero modes. The zero mode eigenstates $|\Psi_0^\pm\rangle$ in valley $K_\pm$ take the form

$$|\Psi_0^+\rangle = \begin{pmatrix} 0 \\ |\varphi_{0,k}\rangle \end{pmatrix}, \quad |\Psi_0^-\rangle = \begin{pmatrix} |\varphi_{0,k}^*\rangle \\ 0 \end{pmatrix}. \tag{14}$$

Noting that in the chiral representation of Hamiltonian (A10) the A and B sublattices are exchanged in the K_- valley, we observe that the zero modes have support on the *same* sublattice (the B sublattice in this case). In case of magnetic LLs, the zero modes have support on opposite sublattices. This is an important characteristic of PLLs that will play a key role in the splitting of PLLs by interactions. Note that time reversal symmetry in the zero mode subspace is preserved by counterpropagation of Landau orbitals in the two valleys: $|\varphi_{0,k}^*\rangle = |\varphi_{0,-k}\rangle$.

In order to gain insight into the effect of symmetry-breaking perturbations on the electronic spectrum of periodic strain superlattices, we review the effect of such perturbations on the PLL spectra for a uniform pseudomagnetic field. Consider the $n = 0$ PLL, the eigenstates of which are given in Eq. (A14). We first comment on the mass terms $\nu^z\tau^z$ and τ^z. The effect of the inversion-symmetry-breaking charge density wave (CDW) $\nu^z\tau^z$ and the time-reversal-symmetry-breaking Haldane term τ^z is reversed as compared to real magnetic fields [23]. The sublattice-polarized CDW simply shifts the energy of zero modes but does not break their degeneracy, whereas the Haldane mass τ^z energetically splits the zero modes in a symmetric way. This is an immediate consequence of the sublattice structure of the PLL zero modes. The two Kekulé masses ν^x and ν^y do not affect the zero modes at all; they are neither split nor shifted, since they are off-diagonal is sublattice space.

Perturbations that do lift the degeneracy of the zero modes are charge density waves with tripled unit cell, i.e., charge density waves that couple the valleys K_+ and K_- [34]. These charge density waves couple to the Dirac matrices $\nu^1\tau^1$, $\nu^1\tau^2$, $\nu^2\tau^1$, and $\nu^2\tau^2$. Projecting these into the PLL zero mode subspace, one finds effective Pauli matrices $\tilde{\tau}^x$ and $\tilde{\tau}^y$, which anticommute with the Haldane mass projected into the zero mode space, $\tau^z \to \tilde{\tau}^z$. This leads to the counterintuitive situation of anticommuting masses only one of which is TRS breaking and nontrivial [51]. We note that these charge density waves with tripled unit cell correspond to the other gauge field components of the SU(2) gauge field; i.e., they enter as $\mathcal{A}_x^1$, $\mathcal{A}_y^1$, $\mathcal{A}_x^2$, and $\mathcal{A}_y^2$ in Eq. (5). Yet another perturbation that splits the zeroth PLL is the valley mass, given by ν^z, making the valleys inequivalent, but acting as the identity in sublattice space. Its spectral effect is equivalent to that of the Haldane term, meaning a symmetric splitting of the zero modes.

Understanding the spectral effect of these Dirac fermion bilinears on the zeroth PLL gives a first idea of the ways in which their spontaneous formation can lower the energy for charge neutral systems. For a more refined understanding of the energetics it is necessary to consider the effect of perturbations on higher PLLs (i.e., $n \neq 0$). For both the CDW term $\nu^z\tau^z$ and the Haldane term τ^z all PLLs with $n \neq 0$ get pushed up or down in energy depending on whether they have energies $\pm\sqrt{2\xi^2 n}$; i.e., positive (negative) solutions get pushed up (down). This is different for the valley mass ν^z, which pushes all PLLs of valley K_+ up and of valley K_- down, effectively splitting all PLLs, even the $n \neq 0$ levels, leaving no degeneracies behind. The charge density waves with enlarged unit cell (i.e., coupling the valleys) both split and shift the higher order PLLs, which may be seen straightforwardly by using perturbation theory up to second order. Based on these considerations we obtain an intuition for the spontaneous generation of Dirac fermion bilinears due to interactions, depending on the location of the Fermi level.

B. Alternating pseudomagnetic fields and superlattice PLLs

The assumption of uniform pseudomagnetic field is a useful first step towards understanding the physics of superlattice PLLs. As a next step we consider the case of alternating pseudomagnetic field, which for simplicity we will take as a periodic arrangement of regions of positive and negative constant field. This will provide valuable insight in the case of periodic harmonic pseudomagnetic fields. Schematically this field arrangement is shown in the top row of Fig. 3. Figure 3 shows how we can think of the periodically alternating field as a strain superlattice with effective "two-site" unit cell (i.e., positive and negative field), reminiscent of an antiferromagnet, leading to a doubling of the PLL degeneracies. For instance, the space of zero mode PLLs is doubled, since we have the

spatial degeneracy in addition to valley degeneracy. For each valley there is a zero mode localized in the positive field region, meaning on the A sublattice, and a zero mode localized in the negative field region, on the B sublattice.

The additional degree of freedom originating from the periodicity of the pseudomagnetic field gives rise to a richer structure of polarized or ordered states. Focusing on the PLL zero mode subspace, relevant at charge neutrality, there are multiple ordered states that lift the degeneracy of the zero mode subspace. Two of them are shown in Fig. 3. The first is a charge ordered state, where the zero mode PLLs in one of the two spatial regions are both occupied, leaving the zero modes in the other region unoccupied. This leads to a redistribution of charge between the two regions and an associated ferroelectric polarization along the propagation direction of the superlattice wave vector. In the case of graphene this state is realized by the sublattice CDW, which energetically discriminates the sublattices. The other state shown in Fig. 3 is the valley-ordered quantum Hall (or Haldane) state. In such state the zero modes corresponding to an "up" pseudomagnetic field are occupied. Note that this implies an alternating occupation of valleys $K_\pm$, as shown in Fig. 3. Therefore, this state may be called *anti-ferro-valley*-ordered. In graphene the valley-ordered quantum Hall state is realized by the time-reversal-symmetry-breaking Haldane term. A third PLL polarized state is obtained by occupying the same valley in each spatial region. This state also breaks time reversal, but contrary to the valley-ordered quantum Hall state the pseudomagnetic field seen by the occupied PLLs alternates. The inversion of PLL occupation in one of the two regions with respect to the anti-ferro-valley-ordered state suggest the name *ferro-valley*-ordered. In graphene such state is realized by the valley mass term.

We now establish a connection between the simplified description of alternating pseudomagnetic fields in terms of continuum PLLs, and the periodic strain (super)lattice model introduced in the previous section. In order to do so we take the unidirectional periodic strain profile compatible with an enlarged six-site unit cell (i.e., Dirac valleys folded onto Γ) defined in Eq. (12). Solving the tight-binding Hamiltonian in the presence of the strain superlattice yields the spectrum shown in Fig. 4 (upper left). The connection is made by interpreting this spectrum in terms of PLLs.

Let us first study the wave function support of the zero energy solutions and compare that to the zeroth PLL. The right column of Fig. 4 shows the wave function support $|\psi^{A,B}_{n=0,k}|^2$ of the wave functions $\psi_{n=0,k}$ corresponding to zero energy solutions ($n = 0$) labeled by k (k should be identified with k_y). Black arrows explicitly indicate which k corresponds to which $|\psi^{A,B}_{n=0,k}|^2$ profile. Since there are two valleys and the strain superlattice unit cell consists of two distinct regions with opposite pseudomagnetic field, there is a fourfold degeneracy at each k. This is reflected in Fig. 4 where two pseudomagnetic Landau-like orbitals are localized on the A sublattice (lower right) and two localized on the B sublattice. The wave function support clearly shows the spatial separation of solutions living on distinct sublattices. In the region of positive field (see Fig. 4, lower left) "zero modes" are localized on the A sublattice, and on the B sublattice in the region of negative field. In addition, we observe that for k moving away from Γ (following the blue arrow) the two Landau orbitals in each region move away

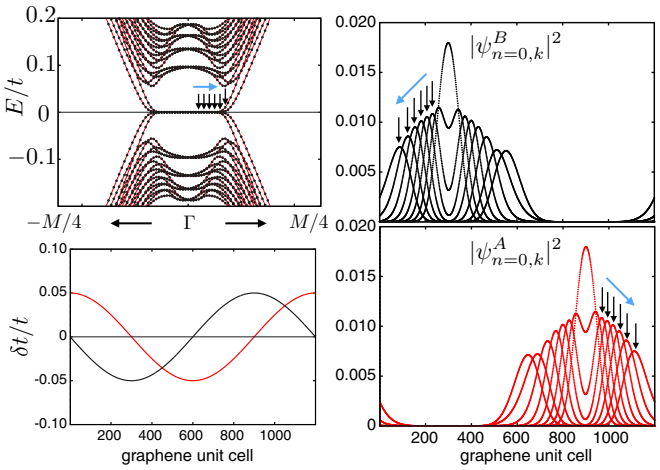

FIG. 4. Upper left: Spectrum in the presence of a strain-induced periodic pseudomagnetic field, shown with both Dirac points folded onto Γ. Periodicity of the pseudomagnetic field is 1200 graphene unit cells, and we used $A = 0.05t$. Black arrows indicate for which k the zero mode eigenstates are plotted in the upper and lower right panels. In these two panels we show the wave function distribution $\sim|\psi^{A,B}_{n=0,k}|^2$ of the full zero mode (i.e., $n = 0$) subspace over the graphene unit cells for the A sublattice (lower right, red) and B sublattice (upper right, black). Black arrows indicate which k they correspond to in the upper left plot; the blue arrow indicates in which order. Lower left: Plot of the periodic strain modulation $\mathcal{A}_x = A\cos(2\pi y/\lambda) \sim 2\delta t_1(y) - \delta t_2(y) - \delta t_3(y)$ (red) and corresponding pseudomagnetic field. Note that for clarity we have rescaled the amplitude of the pseudomagnetic field to A.

from the position of maximum field towards the position of vanishing field. In particular, they move away in opposite directions, which is a direct consequence of their different valley index. As the two valleys effectively see opposite fields, and the spatial position of a Landau orbital is given by $x \propto \mathrm{sgn}(\mathcal{B})k_y$, the Landau orbitals are expected to spatially move in opposite directions. With increasing k ($\sim k_y$) Landau orbitals of different spatial regions and the same valley start to overlap, eventually leading to the splitting observed in spectrum indicated by the most right black arrow in the upper left panel of Fig. 4. Hence, at the junctions between regions of positive and negative field, the Landau orbitals acquire a dispersion and form a series of snake states [30].

Next, we ask what the spectral effect is of the perturbations that are expected to split degeneracies, in particular the flat band degeneracies as depicted in Fig. 3. To this end, we solve the strain superlattice Hamiltonian in the presence of various perturbations, which for the moment we take to be spatially uniform, i.e., not follow the superlattice envelope, in accordance with the schematic picture of alternating regions of constant field (Fig. 3). Figure 5 shows the low-energy spectrum in the vicinity of Γ. The unperturbed case corresponding to $\hat{H}_0 + \hat{H}_{\mathrm{strain}}$ is shown in Fig. 5(a) for reference. The sublattice charge-ordered state and (anti-ferro-)valley-ordered quantum Hall state are shown in Fig. 5(b) and Fig. 5(c), respectively. Both open up a full gap, splitting the zero mode subspace and shifting the higher PLLs, as expected. Figure 5(d) shows the effect of a valley mass term, i.e., the

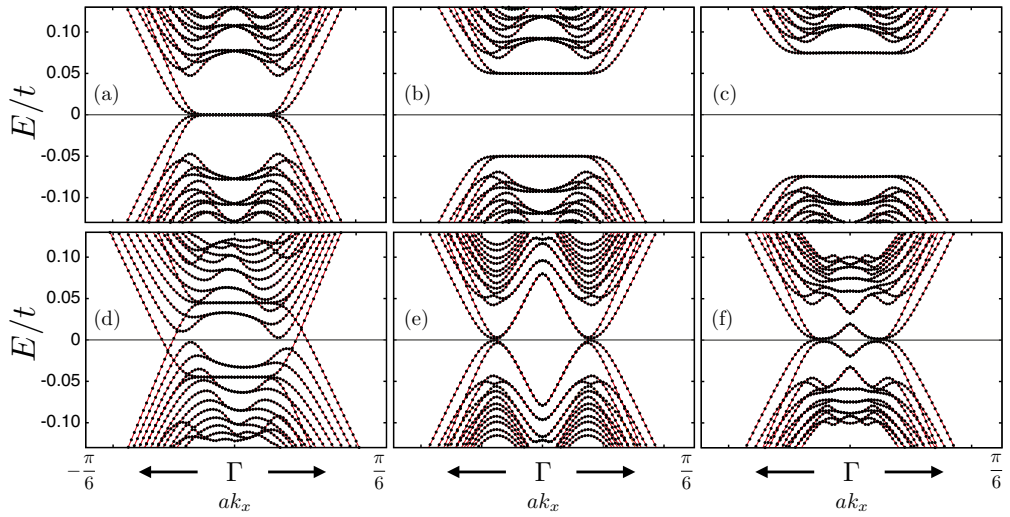

FIG. 5. Spectra of graphene in the presence of periodic strain and in the presence of additional perturbations splitting or lifting PLL energies. Spectra are obtained for strain superlattice unit cells containing $\lambda = 600$ graphene unit cells and $A = 0.08t$. (a) Free graphene, (b) CDW, (c) Haldane term, (d) valley mass term, (e) CDW_1 with tripled unit cell, (f) CDW_2 with tripled unit cell.

ferro-valley-ordered, on the low-energy spectrum. Whereas in each valley degeneracies are preserved, the valleys are split, as expected. As a consequence, the spectrum is not gapped and the Fermi level crosses the propagating snake states associated with the flat band PLLs [30].

Figure 5(e) and 5(f) show the spectrum obtained in the presence of valley-coupling CDWs, which we have discussed split the continuum $n = 0$ PLL in a way similar to the Haldane term. We observe that in the case of a strain superlattice, the CDWs do not lead to a full gap, but only lift the degeneracy of the flat band states localized at the position where the pseudomagnetic field has its extrema. The degeneracy is not lifted in the vicinity of the nodes of the periodic pseudomagnetic field. The absence of a full gap in case of periodic strain can be understood by considering the spectral effect of the valley-coupling CDWs in the case of zero pseudomagnetic field. The valley-coupling CDWs do not open up a gap in that case, but only shift the Dirac points. Hence, at the nodes of the pseudomagnetic field one expects the absence of a gap. Note also that the spectrum obtained numerically shows both split and shifted higher ($n \neq 0$) PLLs.

From this analysis we conclude that in the presence of the strain superlattice, the low-energy electronic structure can be approximated by sets of PLLs for the two distinct regions of the superlattice unit cell. In addition, based on their effect on the degenerate low-energy PLLs, we expect the charge-ordered and anti-ferro-valley-ordered states to be the dominant instabilities in the presence of the pseudomagnetic field superlattice.

We end this section with two remarks. First, we note that the analysis presented here is based on the the assumption of a strain-induced pseudomagnetic field, i.e., $\vec{\mathcal{A}} = \vec{\mathcal{A}}^3$ in Eq. (5). As mentioned in Sec. II, a unitary matrix can rotate to another component, e.g., $\vec{\mathcal{A}}^1$ or $\vec{\mathcal{A}}^2$. This is does not change the (low-energy) spectrum, but it does change the nature of the eigenstates. In addition, it also changes the nature of the perturbations, since the unitary matrix rotates within the space of masses represented by $\vec{\Gamma}$ as well. In particular, this implies that a sublattice-polarized term $\nu^z\tau^z$ will be rotated into one of the Kekulé terms. Interestingly, the Haldane term is a scalar under these unitary rotations and hence is invariant. To summarize, the analysis of this section still applies, but in a rotated basis.

The second remark concerns the applicability of our analysis to TCI surface states. The arguments put forward in the present section build on the specific example of graphene PLL physics. They remain valid in the context of TCI surface states. Most importantly, in the presence of a uniform pseudomagnetic field, the TCI surface $n = 0$ PLLs are localized on the TCI pseudospin degree of freedom in such a way that the time-reversal-invariant ferroelectric distortion of the crystal lattice only shifts them, whereas a time-reversal-breaking Zeeman-type spin coupling splits them in energy. As a result, there is a one-to-one correspondence between the valley-ordered quantum Hall state and charge-ordered state in graphene, and the Zeeman term and ferroelectric distortion of TCI surface states.

V. INTERACTING ELECTRONS IN A STRAIN SUPERLATTICE

In order to systematically investigate the patterns of symmetry breaking and PLL splitting resulting from interacting flat band electrons, we have studied an interacting electron Hamiltonian on the graphene honeycomb lattice and performed extensive self-consistent Hartree-Fock calculations. We report the results in this section.

Based on the intuitive picture of the PLLs in the two spatially separated regions, we anticipate both the formation of a charge-ordered state with ferroelectric polarization (corresponding to a redistribution of charge between the regions of positive and negative pseudomagnetic field) and the formation of a valley-ordered quantum Hall ground state (i.e., the anti-ferro-valley polarized state, see Fig. 3). Interactions which, within a mean-field treatment, can give rise to the formation of these states in a graphene lattice model

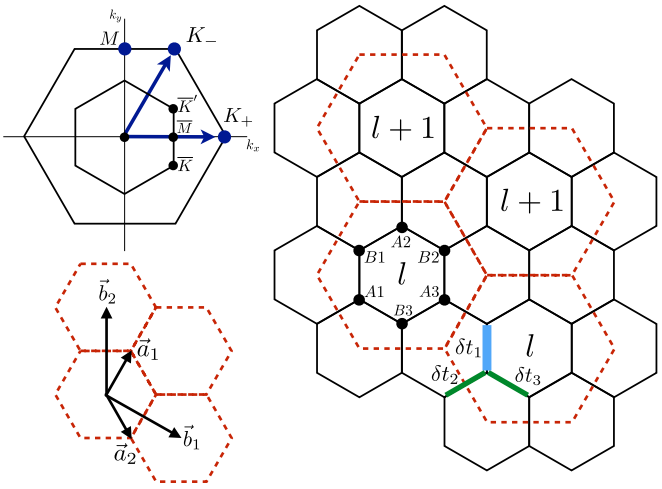

FIG. 6. Upper left: Schematic representation of the graphene Brillouin zone (outer black hexagon) and the folded Brillouin zone corresponding to the tripled unit cell (inner black hexagon). Dirac points of pristine graphene are located at K_+ and K_-, which are folded onto Γ when tripling the unit cell. The vectors connecting Γ to K_+ and K_-, indicated by blue arrows, are reciprocal lattice vectors of the enlarged lattice vectors. Lower left: Wigner-Seitz cells containing three elementary graphene unit cells, with lattice vectors $\vec{a}_1$ and $\vec{a}_2$. Right: Graphene lattice (black hexagons) and tripled unit cells (red dashed hexagons), including labeling of sites. Ai and Bi label the six sites within the enlarged unit cell; l and $l+1$ label the position in the strain-induced superlattice. $\delta t_{n=1,2,3}$ are the hopping amplitude changes due to strain.

are the nearest-neighbor (NN) and next-nearest-neighbor (NNN) density-density interactions [37], respectively, as will be demonstrated below. We therefore consider a minimal interacting electron Hamiltonian $\hat{H}$ which can capture all the physics described in Sec. IV. Specifically, the Hamiltonian is given by $\hat{H} = \hat{H}_0 + \hat{H}_{\vec{\mathcal{A}}} + \hat{H}_{\rm int}$ where $\hat{H}_0$ is the kinetic term describing free electrons hopping on the honeycomb lattice, $\hat{H}_{\vec{\mathcal{A}}}$ describes the strain superlattice, and the interacting part $\hat{H}_{\rm int}$ takes the form

$$\hat{H}_{\rm int} = V_1 \sum_{\langle rr'\rangle} \hat{n}_r \hat{n}_{r'} + V_2 \sum_{\langle\langle rr'\rangle\rangle} \hat{n}_r \hat{n}_{r'}. \tag{15}$$

Here V_1 is the NN interaction strength and V_2 the NNN interaction strength, and $\hat{n}_r$ is the density operator at site r. The sums over $\langle rr'\rangle$ and $\langle\langle rr'\rangle\rangle$ are over NNs and NNNs, respectively.

A schematic representation of the way we set up the numerical Hartree-Fock calculations is given in Fig. 6, which is a generalization of the approach of Ref. [38] to the case of strain superlattices (see Appendix B for more details). In order to allow for charge density waves that couple the Dirac points K_+ and K_- we work with an elementary graphene unit cell containing *six* sites, i.e., a tripled unit cell, instead of the minimal two-site unit cell (red dashed hexagons in Fig. 6) [38]. With this choice of unit cell we explicitly allow for all possible interaction-induced charge or bond density modulations with a periodicity corresponding to wave vectors K_+ and K_-. Since these are also the wave vectors connecting the Dirac points (and hence the PLLs), we allow for both intravalley and intervalley coupling. As a result, our numerical calculations can discriminate all possible polarized states. The lattice vectors corresponding to the six-site unit cell are $\vec{b}_1 = 2\vec{a}_2 + \vec{a}_1$ and $\vec{b}_2 = \vec{a}_1 - \vec{a}_2$, where $\vec{a}_{1,2}$ are the graphene lattice vectors connecting NNNs (see Fig. 6). Within each six-site unit cell we label the sites by an index $\alpha = A,B$ denoting the sublattices, and an index $i = 1,2,3$ denoting the three sites of each sublattice flavor; see Fig. 6. Electron annihilation (creation) operators are given by $\hat{\psi}_{\alpha i}$ ($\hat{\psi}^\dagger_{\alpha i}$).

The spatially modulated strain is implemented in the way described in Sec. III, Eqs. (10) and (12). Specifically, we take the strain superlattice Hamiltonian $\hat{H}_{\vec{\mathcal{A}}}$ to describe a pseudomagnetic gauge field $\vec{\mathcal{A}} = (\mathcal{A}_x, 0)$, where the $\mathcal{A}_x$ component of the gauge field originating from hopping amplitude modulations $\mathcal{A}_x \sim 2\delta t_1 - \delta t_2 - \delta t_3$ [see Eq. (10)]. The pseudomagnetic field is induced by giving the hopping amplitude modulations a spatial dependence: $\delta t_{n=1,2,3} \to \delta t_{n=1,2,3}(\vec{r})$. We take the strain-induced gauge field to be

$$\mathcal{A}_x(\vec{r}) = A\cos\left(\frac{\vec{K}\cdot\vec{r}}{\lambda/3}\right), \tag{16}$$

where, importantly, $\vec{r}$ denotes the position of a two-site (minimal) graphene unit cell, and $\vec{K}$ is the K_- wave vector as shown in Fig. 6. Here, λ equals the size of the strain superlattice unit cell, i.e., the number of graphene unit cells in the periodic strain superlattice unit cell. This implies that the number of six-site unit cells in the superlattice unit cell is $\lambda/3$. As a result, the lattice vectors of the superlattice are $\vec{b}_1$ and $\lambda\vec{b}_2/3$. We introduce an additional index $l = 1,\ldots,\lambda/3$ to label the six-site unit cells in the strain superlattice unit cell. The electron operators within a superlattice unit cell are then denoted as $\hat{\psi}_{\alpha i}(l)$. The strain superlattice endows the system with a (superlattice) periodicity, and we take the Fourier transform with respect to the superlattice unit position, yielding electron operators $\hat{\psi}_{\alpha i}(l,\vec{k})$. Here, $\vec{k}$ takes values in the mini-BZ defined by reciprocal superlattice vector. This defines the setup of our calculations.

Spinless electrons on the graphene honeycomb lattice serve as a model system for strain-induced PLLs. We therefore focus on the Hartree-Fock results for spinless electrons and then briefly comment on the spin degree of freedom, recalling that the case of TCI surface states is similar to spinless graphene electrons.

A. Spinless electrons

We start by defining the relevant order parameters. Within the framework of standard Hartree-Fock theory we decouple the interactions, defined in Eq. (15), both in diagonal (Hartree) and off-diagonal (Fock) channels. The diagonal or charge density order parameter at a given site in the superlattice unit cell is labeled by (α,i,l) and is defined as

$$\rho_{\alpha i}(l) = \frac{1}{N}\sum_{\vec{k}} \langle \hat{\psi}^\dagger_{\alpha i}(l,\vec{k})\hat{\psi}_{\alpha i}(l,\vec{k})\rangle. \tag{17}$$

Recall that $\alpha = A,B$, $i = 1,2,3$, and l labels the six-site cell in the superlattice cell. Here, N is the total number of superlattice unit cells. We define $\rho_\alpha(l)$ as the average of $\rho_{\alpha i}(l)$ within each

superlattice cell labeled by l

$$\rho_\alpha(l) = \frac{1}{3}\sum_{i=1}^{3}\rho_{\alpha i}(l). \tag{18}$$

Based on the considerations of Sec. IV, we are interested in possible local sublattice imbalances $\Delta_{\rho-}(l)$ defined as

$$\Delta_{\rho-}(l) = \rho_A(l) - \rho_B(l). \tag{19}$$

Hence, $\Delta_{\rho-}(l)$ is the CDW order parameter as a function of the index l. To a detect a possible ferroelectric redistribution of charges between regions of positive and negative pseudomagnetic field, we define the order parameter $\Delta_{\rho+}(l)$ given by

$$\Delta_{\rho+}(l) = \rho_A(l) + \rho_B(l) - 1. \tag{20}$$

The order parameter $\Delta_{\rho-}(l)$ describes charge redistribution within a six-site unit cell, whereas $\Delta_{\rho+}(l)$ describes charge within the (strain) superlattice unit cell, i.e., between six-site unit cells.

In addition to the charge density order parameter, we study the quantum Hall (QH) order parameter $\Delta_{\rm QH}$ describing spontaneously generated next-nearest-neighbor hopping with complex amplitude. The order parameter $\Delta_{\rm QH}$ serves to detect the anti-ferro-valley polarized state of the previous section, and is associated with a spontaneous quantum Hall effect. Since microscopically it originates from complex hoppings, it is an off-diagonal or bond order parameter. Therefore, in order to write down an expression for $\Delta_{\rm QH}$ we define the NNN bond hopping expectation values $\chi^{\alpha}_{il,jl'}$ for each sublattice α as

$$\chi^{\alpha}_{il,jl'} = \frac{1}{N}\sum_{\vec{k}} \mathcal{Q}^{\alpha *}_{il,jl'}(\vec{k})\langle\hat{\psi}^{\dagger}_{\alpha i}(l,\vec{k})\hat{\psi}_{\alpha j}(l',\vec{k})\rangle, \tag{21}$$

where (il) and (jl') are NNN. The phase factors $\mathcal{Q}^{\alpha}_{il,jl'}(\vec{k})$ arise when (il) and (jl') are in different superlattice unit cells, and they are explained in more detail in Appendix B. From this set of NNN hopping expectation values, we extract the QH order parameter $\Delta_{\rm QH}(l)$ by taking

$$\Delta_{\rm QH}(l) = \sum_{ijl'\in {\rm NNN}(l)} \eta_\alpha {\rm Im}\ \chi^{\alpha}_{il,jl'}. \tag{22}$$

Here, the sum is over all NNN pairs which belong to cell l and $\eta_A = -\eta_B = 1$ since in the QH Haldane state the fluxes on the A and B sublattices have opposite sign.

The representative results of the self-consistent HF calculations we will now present were obtained for spinless electrons on lattices of size $N = 16\times 16$ and $\lambda = 3\times 40 = 120$. We have verified these results for various superlattice unit cell sizes. In the following we map out the phase diagram as a function of V_1 and V_2 by discussing the results for three specific regimes separately. First we will focus on $(V_1 = 0, V_2 \neq 0)$ to show that the QH state is stabilized for the smallest values of V_2 as a result of the strain-induced flat PLL-like bands. Second, we will look at the case $(V_1 \neq 0, V_2 = 0)$ to show that a NN interaction will induce the ferroelectric charge-ordered state. Third and last we will focus on selected cases of $(V_1 \neq 0, V_2 \neq 0)$ to show that the ferroelectric charge density wave is strongly suppressed as compared to the valley-ordered QH state, precisely due to the localization of the low-energy flat band states on a single sublattice.

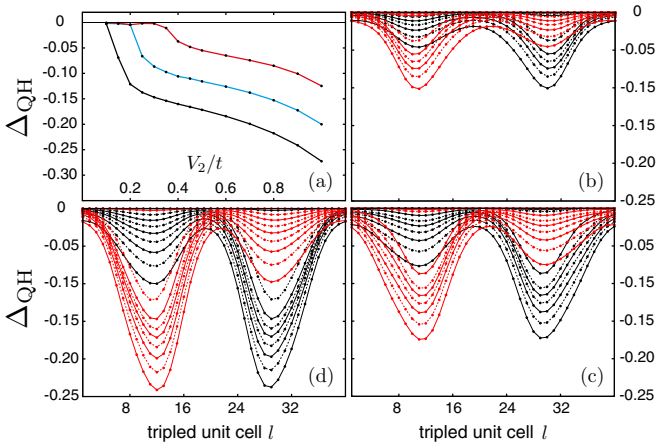

FIG. 7. Panel (a) shows the maxima of QH order parameter $\Delta_{\rm QH}$ as function of NNN interaction V_2 for various values of the pseudomagnetic field amplitude: $A = 0.10$ (red), $A = 0.15$ (blue), $A = 0.20$ (black). Panels (b) and (c) show the QH order parameter as function of tripled unit cell $\Delta_{\rm QH}(l)$ (l labeling tripled unit cell) for the same values of A [(b) $A = 0.10$; (c) $A = 0.15$; (d) $A = 0.20$]. Curves are shown for $V_2 = 0.1, 0.2, 0.3, 0.4, 0.5, 0.6, 0.7, 0.8, 0.9, 1.0$, in descending order, i.e., bottommost curves $V_2 = 1.0$ and topmost curves $V_2 = 0.1$. Black and red curves correspond to A and B sublattice, respectively. $V_1 = 0$ in all cases.

Figure 7 shows the HF results for various values of NNN interaction V_2 while keeping $V_1 = 0$. Panels (b) and (c) show the QH order parameter $\Delta_{\rm QH}(l)$ defined in Eq. (22) as function of then tripled cell index l. Black and red curves correspond to the A and B sublattices, respectively, and the strength of the tunneling amplitude variation A is $A = 0.10$ (b), $A = 0.15$ (c), and $A = 0.20$ (c). It is apparent from these panels that the QH order parameter follows the profile of the effective pseudomagnetic field. In the spatial region where the flat band states are localized on the A sublattice, the QH order parameter develops predominantly on the A sublattice, and vice versa for the B sublattice region. Ordinarily, in the honeycomb lattice QH state, the spontaneously induced magnetic fluxes are opposite on the A and B sublattices, averaging to zero over an elementary unit cell [7]. In the present case the localization of flat band states on a single sublattice leads to finite fluxes in regions of positive and negative pseudomagnetic field, which average to zero only over the larger strain superlattice unit cell.

In addition to the locking of the QH order parameter $\Delta_{\rm QH}(l)$ to the sublattice structure of the flat band zero modes, we observe that the strain-induced reorganization of the low-energy electronic structure into PLLs fundamentally changes the impact of interactions. Figure 7(a) shows the dependence of the QH order $\Delta_{\rm QH}(l_{\rm max})$, where $l_{\rm max}$ is the cell index where the QH order is strongest, on the strength of the interaction V_2 for various values of the pseudomagnetic field strength (i.e., A). Whereas for the unstrained honeycomb lattice a finite interaction $V_2 \sim 1.3$ is needed to stabilize the QH state (within HF theory) [37–39] due to the vanishing density of states at half filling, here we find that the QH state is induced already for small interactions, in particular in regions where the effective field is strongest. For perfectly flat bands such as PLLs one expects the interaction-induced order to scale linearly with

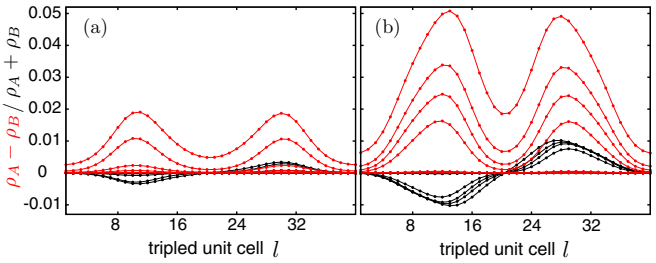

FIG. 8. (a) Plots of the charge density wave order parameter $\rho_A(l) - \rho_B(l)$ (red) and total charge redistribution $\rho_A(l) + \rho_B(l) - 1$ (black) for values of the NN interaction $V_1 = 0.2, 0.4, 0.5, 0.6, 0.7, 0.8$, in both cases plotted in ascending order (top curve $V_1 = 0.8$, bottom $V_1 = 0.2$); $A = 0.10$. (b) Same as (a) but with $A = 0.20$.

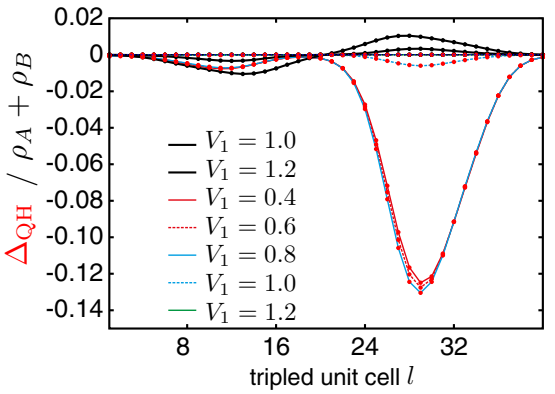

FIG. 9. Plot of both the QH order parameter $\Delta_{\mathrm{QH}}(l)$ (only A sublattice shown; red dotted curves) and total charge redistribution $\rho_A(l) + \rho_B(l) - 1$ (black dotted curves) as a function of tripled unit cell index n for $A = 0.20$ and $V_2 = 0.20$. Different curves correspond to different values of V_1, explicitly labeled for clarity.

interaction for weak coupling [52,53]. This is reflected in Fig. 7(a) which shows that for increasing pseudomagnetic field, setting the PLL band flatness, the QH is more robust and its dependence on the interaction is approximately linear, with deviations at very small values of V_2.

Next, we turn to the case of finite NN interaction V_1 while keeping $V_2 = 0$. In the absence of strain the unfrustrated NN interaction will favor a CDW characterized by translational-symmetry-preserving sublattice charge imbalance [37–39]. On the contrary, in the presence of strain, adopting the PLL picture for the low-energy electrons and focusing on the zeroth PLL, the effect of the NN interaction is expected to be suppressed, as the zeroth PLL states live exclusively on one sublattice. Nevertheless, since the NN has the potential to cause charge asymmetry between the sublattices (i.e., the regions of positive and negative pseudomagnetic field), and higher PLLs may be relevant to the energetics, we anticipate the system to develop a charge density wave of ferroelectric type (i.e., $\Delta_{\rho+}$), with excess charge in regions where the pseudomagnetic field is positive, and defect charge where it is negative, or vice versa. In addition, in the previous section we observed that under the assumption of a uniform CDW the strain-induced PLL spectrum is gapped out.

In Fig. 8 we show results for both $\Delta_{\rho+}(l)$ and $\Delta_{\rho-}(l)$, defined in Eqs. (20) and (19), for different values of the interaction V_1 and strain A. As expected, we find the CDW order parameter $\Delta_{\rho-}(l)$ (shown in red) to become finite in regions where the pseudomagnetic field is strongest, but to have the same sign in both positive and negative regions. The sign of concomitant ferroelectric polarization depends on the sign of the pseudomagnetic field. In the region where the field is positive the flat band states are localized on the A sublattice and pushing them down in energy, signaled by positive $\Delta_{\rho-}(l)$, leads to excess charge in that region at the expense of charge in the region of negative field. At the same time we observe that the FP is more pronounced for stronger strains, and that it is very weak for small interaction. The latter may be attributed to the fact that NN interactions have no effect in the zeroth PLL.

We proceed to consider the case of both finite V_1 and V_2. We have seen that both of these interaction individually favor different gapped ground states. At the same time we argued that as a consequence of the different nature of these interactions, i.e., V_1 being inter-sublattice and V_2 being intra-sublattice, they have different impact on the low-energy flat band electrons. Due to the spatial separation of states localized on different sublattices, it is expected that the effect of V_1 is suppressed. One therefore expects the QH state to survive even for $V_2 < V_1$, which corresponds to the physically relevant regime.

In Fig. 9 we present results for various V_1 with finite $V_2 = 0.2$ and for $A = 0.20$. We plot both the ferroelectric order parameter $\Delta_{\rho+}(l)$ and the QH order parameter $\Delta_{\mathrm{QH}}(l)$ for the A sublattice. The key observation is that even for small $V_2 = 0.2$ the QH survives up to NN interactions $V_1 \sim 1.0$. We therefore conclude that the effect of interactions on periodic-strain-induced flat bands follows from their PLL character. In particular, the sublattice structure of the low-energy flat bands is the decisive factor in determining which order is spontaneously generated by interactions.

B. Remarks on spinful electrons

We close this section with a number of remarks on the electron spin. The numerical calculations have been performed for spinless electrons in graphene. Taking spin into account gives rise to a richer structure of polarized states; specifically the ferromagnetically (FM) and antiferromagnetically (AFM) polarized states should then be considered, in addition to the Quantum Spin Hall polarized state. Moreover, the argument for the suppression of the NN interactions does not apply to the on-site Hubbard interaction, $\hat{H}_U = U \sum_r \hat{n}_{\uparrow r} \hat{n}_{\downarrow r}$, which must be included in the interacting Hamiltonian.

The results for spinless electrons in graphene do, however, directly apply to TCI surfaces, which do not have an additional degenerate spin degree of freedom. Instead, as a consequence of spin-orbit coupling, spin is already part of the low-energy Dirac structure. In particular, our results imply that on the surface of a TCI and in the presence of periodic strain, interactions will lead to the formation of the QH state.

As a first step towards understanding the polarization of spinful strain superlattice-induced PLLs in graphene, we have performed numerical Hartree-Fock calculations with an interacting Hamiltonian given by H_U. We find that the mean-field ground is a *superlattice antiferromagnet*, as shown in Fig. 10.

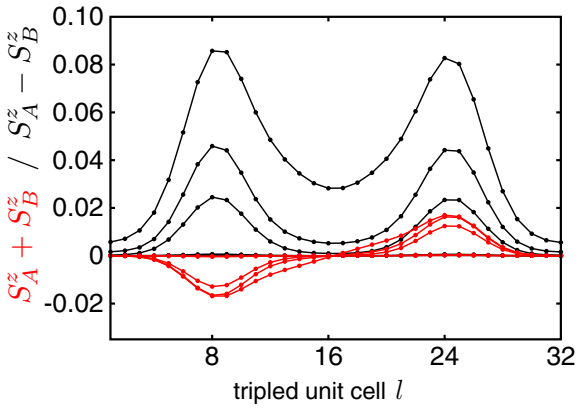

FIG. 10. Plots of the Néel order parameter $S_A^z(l) - S_B^z(l)$ and magnetization $S_A^z(l) + S_B^z(l)$ as a function of six-site unit cell index l. For the spinful calculations we have used a strain superlattice with wavelength $\lambda/3 = 32$ ($l = 1, \ldots, 32$). The results were obtained for $V_1 = V_2 = 0$, $A = 0.15$, and different curves correspond to $U = (0.4, 0.8, 1.2, 1.6, 2.0)$. These results show that in addition to local antiferromagnetic order $S_A^z(l) - S_B^z(l)$ a superlattice antiferromagnetic order [signaled by $S_A^z(l) - S_B^z(l)$] develops as a result of the localization of the zero mode eigenstates.

The superlattice antiferromagnet exhibits antiferromagnetic order defined by $S_A^z(l) - S_B^z(l)$, as expected on a bipartite honeycomb lattice, where $S_\alpha^z(l)$ is the spin density along z on the α sublattice as function of the index l. Since, however, the flat band states are localized on one sublattice only, in each of the two regions of the strain superlattice an effective magnetization develops, given by $S_A^z(l) + S_B^z(l)$. $S_A^z(l) + S_B^z(l)$ has opposite sign in the two regions of the superlattice unit cell which see opposite pseudomagnetic field. Hence, as a consequence of the particular structure of the zeroth PLL states, the antiferromagnetic order is transferred to the superlattice.

A similar result was reported in Ref. [28], which found antiferromagnetic order induced by nonperiodic strain, where the bulk and the sample boundary have an effective but opposite magnetization.

VI. DISCUSSION AND CONCLUSION

We have shown that in the presence of a strain superlattice, a periodic modulation of elastic lattice deformations, a system of low-energy Dirac electrons exhibits a fourfold-degenerate zero energy flat band, reminiscent of a zeroth PLL. The PLL structure originates from the pseudomagnetic field, generated by nonuniform strain. The strain superlattice unit cell consists of two spatially distinct regions, one in which electrons see a positive pseudomagnetic field and one in which they see a negative field. The single-particle states of the degenerate flat band have a special and important localization property: in each of the two regions their wave function has support only on one of the Dirac pseudospin species.

Periodic pseudomagnetic fields can occur both in graphene and on the surface of a TCI, which hosts pairs of Dirac fermions at opposite momenta related by time reversal symmetry. The important fact that Dirac fermions are unpinned to time-reversal-invariant momenta in the BZ allow for pseudogauge field under time-reversal-invariant perturbations such as strain.

Interactions between electrons in continuum PLLs are expected to lead to the formation of polarized states splitting the degeneracies of PLLs. We have investigated PLL polarization for the case of lattice PLLs corresponding to periodic pseudomagnetic fields. Two polarized states were shown to fully lift the zero energy flat band degeneracy while at the same time pushing all occupied (unoccupied) lattice PLLs down (up). The first state is the sublattice-polarized charge-ordered state, which can be pictured as a spatially polarized state with all PLLs of the positive (or negative) field region occupied. The second is the anti-ferro-valley ordered state, or spontaneous quantum Hall state, for which all PLL states effectively seeing a positive (or negative) field are occupied, implying time reversal symmetry breaking. We found that other polarized states, even though they have similar characteristics in the continuum, do not fully lift the lattice flat band PLL degeneracies.

Using self-consistent Hartree-Fock calculations we have studied an interacting honeycomb lattice model with periodic strain-induced lattice PLLs. Our results demonstrate that the strain-induced reconstruction of low-energy electronic structure, in particular the presence of a zero energy flat band, determines the impact of interactions. Three key results highlight this conclusion. First, the mean-field order parameters clearly reflect the periodicity of the pseudomagnetic field, showing that the amplitude of the order parameter is tied to the strength of pseudomagnetic field.

Second, as a consequence of the characteristic wave function support of the flat band single-particle states, the effect of interactions that favor time-reversal-invariant pseudospin order is suppressed. This effectively enhances interactions that favor time-reversal-symmetry-breaking valley order with associated spontaneous quantum Hall effect. We have established this result in the context of the graphene lattice model, where the pseudospin corresponds to the sublattice degree of freedom. The NN interactions are inter-sublattice interactions, and therefore suppressed, as the flat band single-particle states have support on one of the sublattices only, in each positive or negative field region. The result, however, is general and applies equally to TCI surface states. The physical interpretation of pseudospin and valley are different, as explained in Sec. II, yet the effect of interactions favoring time reversal symmetry breaking remains strongly enhanced.

Third, the valley-ordered spontaneous quantum Hall state already occurs for small interactions when the PLLs are well developed. The PLL structure is a way to significantly enhance density of states near the charge neutral point. We conclude that in the presence of periodic strain and interactions, a system of unpinned Dirac electrons has a generic instability towards a spontaneous quantum Hall phase.

The emphasis of the numerical calculations we report, has been on spinless electrons in graphene. In TCI surface states, however, no additional spin degeneracy is present. Due to spin-orbit coupling the electron spin is an intrinsic part of the low-energy Dirac structure. In particular, this implies that there are no purely spin-polarized phases, such as the global antiferromagnet, competing with the spontaneous quantum Hall phase, favoring the latter as ground state.

Whereas uniform strain-induced pseudomagnetic fields suffer from implementation limitations, particularly beyond the nanoscale, periodic strain can potentially be realized in macroscopic sample sizes. In fact, such periodic strain fields and induced pseudomagnetic fields were demonstrated in TCI heterostructures [32,33], making TCI surface states the prime candidate to exhibit spontaneous formation of nontrivial electronic states.

ACKNOWLEDGMENTS

We thank Evelyn Tang, Vladyslav Kozii, and Sarang Gopalakrishnan for interesting discussions. J.V. acknowledges support from the Netherlands Organization for Scientific Research (NWO). L.F. is supported by the David and Lucile Packard Foundation.

APPENDIX A: LANDAU LEVELS FOR DIRAC ELECTRONS

For the purpose of being self-contained we collect some standard results of Dirac fermions in a constant magnetic field in this appendix. These may be directly applied to the case of time-reversal-invariant pseudomagnetic fields, bearing in mind the key characteristic of opposite sign of the pseudomagnetic field in the two valleys.

1. Magnetic Landau levels

In the presence of a magnetic field we define the dynamical momenta using the Peierls substitution

$$\hat{p}_\alpha \;\rightarrow\; \hat{\Pi}_\alpha = \hat{p}_\alpha - eA_\alpha(\hat{r}) = -i\hbar\partial_\alpha + |e|A_\alpha(\hat{r}),$$

where $\hat{p}_\alpha$ is the momentum operator and $\alpha = x,y$ (we restrict the description to two dimensions). $\hat{r}_\alpha$ are the position operators obeying $[\hat{r}_\alpha,\hat{p}_\beta] = i\hbar$ and $A_\alpha(\hat{r})$ is the electromagnetic gauge field. In a magnetic field the momentum operators $\hat{\Pi}_\alpha$ do not commute but instead obey the canonical commutation relation

$$\begin{aligned}[\hat{\Pi}_\alpha,\hat{\Pi}_\beta] &= |e|[\hat{p}_\alpha,A_\beta(\hat{r})] + |e|[A_\alpha(\hat{r}),\hat{p}_\beta] \\ &= -i\hbar|e|F_{\alpha\beta},\end{aligned}$$

where $F_{\alpha\beta} = \partial_\alpha A_\beta - \partial_\beta A_\alpha$ is the field strength. Assuming a uniform field strength in the $\hat{z}$ direction the magnetic field is given by $B_\lambda = \epsilon_{\lambda\mu\nu}F_{\mu\nu}/2$, implying that $F_{\mu\nu} = \epsilon_{\mu\nu\lambda}B_\lambda$. In particular we have for a uniform field $B \equiv B_z$ in the $\hat{z}$ direction,

$$[\hat{\Pi}_\alpha,\hat{\Pi}_\beta] = -i\hbar|e|\mathrm{sgn}(B)B\epsilon_{\alpha\beta z}. \tag{A1}$$

In this expression we have explicitly separated the sign of the magnetic field from its strength $B = |B|$ so as to make dependencies on the sign of the field transparent. Defining the fundamental characteristic length scale in the system, the magnetic length, as $l_B = \sqrt{\hbar/(|e|B)}$, we can write $[\hat{\Pi}_\alpha,\hat{\Pi}_\beta] = -i\hbar^2\mathrm{sgn}(B)\epsilon_{\alpha\beta z}/l_B^2$. This implies a canonical commutation relation between the dynamical momenta and inspires us to define creation and annihilation operators in the usual way as

$$\begin{aligned}\hat{a}^\dagger &= \frac{l_b}{\sqrt{2}\hbar}[\hat{\Pi}_x + i\,\mathrm{sgn}(B)\hat{\Pi}_y], \\ \hat{a} &= \frac{l_b}{\sqrt{2}\hbar}[\hat{\Pi}_x - i\,\mathrm{sgn}(B)\hat{\Pi}_y],\end{aligned} \tag{A2}$$

which obey $[\hat{a},\hat{a}^\dagger] = 1$. Note that the definition of these operators depends on the sign of the B field, which is a direct consequence of Eq. (A1). We note in passing that all of the above did not require specifying a gauge for A_α.

The Landau level spectrum of a Dirac Hamiltonian of the form

$$\mathcal{H} = \hbar v_F(\Gamma_x q_x + \Gamma_y q_y)$$

is then straightforwardly obtained by making the substitution $\hbar q_\mu \rightarrow \hat{\Pi}_\mu$. Squaring the Hamiltonian yields

$$\begin{aligned}\mathcal{H}^2 &= v_F^2\left(\hat{\Pi}_x^2 + \hat{\Pi}_y^2\right) + v_F^2[\hat{\Pi}_x,\hat{\Pi}_y]\Gamma_x\Gamma_y \\ &= \frac{v_F^2\hbar^2}{l_b^2}[2\hat{a}^\dagger\hat{a} - 1 + \mathrm{sgn}(B)\tau_z].\end{aligned}$$

We use that $\hat{a}^\dagger\hat{a} = n$ for standard oscillator wave functions φ_n, i.e., $\hat{a}^\dagger\hat{a}\varphi_n = n\varphi_n$, $\hat{a}\varphi_n = \sqrt{n}\varphi_{n-1}$, and $\hat{a}^\dagger\varphi_n = \sqrt{n+1}\varphi_{n+1}$. One therefore obtains the Landau level energies

$$E_\pm(n) = \pm\sqrt{2\xi^2 n}, \quad n = 1,2,\ldots, \quad \xi^2 \equiv \frac{v_F^2\hbar^2}{l_b^2}. \tag{A3}$$

Each of the $E_\pm(n)$ is twofold degenerate because of the valley degree of freedom, in addition to an $N_\phi = A/2\pi l_b^2$ degeneracy where A is the area of the system.

We find the corresponding eigenstates by taking a closer look at the explicit expression for the Hamiltonian in each valley. Writing $\mathcal{H}_\nu$ for the Hamiltonian in valley $\nu = \pm$ we have

$$\mathcal{H}_\nu = \nu\begin{pmatrix} & \sqrt{2}\xi\hat{a} \\ \sqrt{2}\xi\hat{a}^\dagger & \end{pmatrix}.$$

The eigenstates belonging to the eigenvalues $E_\pm(n)$ of Eq. (A3) are easily obtained as

$$|\Psi_{n\nu\pm}\rangle = \frac{1}{\sqrt{2}}\begin{pmatrix} |\varphi_{n-1,k}\rangle \\ \pm\nu|\varphi_{n,k}\rangle\end{pmatrix}. \tag{A4}$$

In addition to the states $|\Psi_{n\nu\pm}\rangle$ ($n = 1,2,\ldots$) there are also zero mode states $|\Psi_{0\nu}\rangle$, one for each valley, which have zero energy ($E_0 = 0$). Inspecting of Eq. (A13) reveals that these states are given in each of the valleys as

$$|\Psi_{0\nu}\rangle = \begin{pmatrix} 0 \\ |\varphi_{0,k}\rangle\end{pmatrix}. \tag{A5}$$

We stress that this implies the zero modes are localized on *opposite* sublattices for the two valleys, as we had exchanged sublattices for the $\vec{K}_-$ valley.

We proceed to consider the effect of symmetry-breaking terms on the Landau level spectrum. Specifically, we consider first the set of time-reversal-symmetry-invariant masses $\vec{m}$ which enter the Hamiltonian as

$$\mathcal{H}_{\vec{m}} = \vec{m}\cdot\vec{\Gamma} = m_1\nu^x + m_2\nu^y + m_3\nu^z\tau^z,$$

with $\vec{\Gamma} = (\nu^x, \nu^y, \nu^z\tau^z)$. For small masses we may use perturbation theory to study the splitting or shifting of Landau levels. It turns out however that the exact energies can be obtained in the presence of $\mathcal{H}_{\vec{m}}$. The energies are found by squaring the Hamiltonian $\mathcal{H} = \mathcal{H}_0 + \mathcal{H}_{\vec{m}}$, which gives

$$\begin{aligned}\mathcal{H}^2 &= v_F^2\left(\hat{\Pi}_x^2 + \hat{\Pi}_y^2\right) + v_F^2[\hat{\Pi}_x, \hat{\Pi}_y]\Gamma_x\Gamma_y + m^2 \\ &= \frac{v_F^2\hbar^2}{l_b^2}[2\hat{a}^\dagger\hat{a} - 1 + \mathrm{sgn}(B)\tau_z] + m^2,\end{aligned}$$

where we use the anticommutation relations of the Γ matrices. We directly find the energies

$$E_\pm(n) = \pm\sqrt{2\xi^2 n + m^2}, \quad n = 1,2,\ldots. \tag{A6}$$

Expanding the square root $\sqrt{2\xi^2 n}\sqrt{1 + m^2/2\xi^2 n}$ in small $m^2/2\xi^2 n$ yields the same result as second-order perturbation theory.

The Landau level spectrum in the presence of masses can alternatively be obtained by using the relation $[\Omega^i, \Gamma_j] = 2i\epsilon_{ijk}\Gamma_k$ to construct a unitary matrix U which rotates the vector $\vec{m}$ so that one has $U^\dagger\vec{m}\cdot\vec{\Gamma}U = m\Gamma_3$, with $m = |\vec{m}|$. Such transformation block-diagonalizes the Hamiltonian and we obtain the energies in a more direct way. In particular, we can employ the unitary rotation to find the energies of the zero modes for the case of massive Dirac fermions. In the rotated basis we can construct zero mode states in the same way as before, which will have energies

$$E_{0\nu} = -\nu m, \tag{A7}$$

where $\nu = \pm$ represents the valley degree of freedom.

We conclude by taking into account the time-reversal-symmetry-breaking but chiral-symmetry-preserving mass η entering as $\mathcal{H}_\eta = \eta\tau^z$. Since this term is a scalar under chiral rotations generated by Ω^i we may consider $\mathcal{H} = \mathcal{H}_0 + \mathcal{H}_{\vec{m}} + \mathcal{H}_\eta$ and use the chiral rotation U to block-diagonalize the Hamiltonian. The total mass term then is $m\nu^z\tau^z + \eta\tau^z$, which directly leads to the energies

$$E_{\nu\pm}(n) = \pm\sqrt{2\xi^2 n + (\nu m + \eta)^2} \tag{A8}$$

for the Landau levels $n = 1,2,\ldots$. The presence of both of these masses leads to a splitting of Landau levels, whereas the presence of either only shifts the energies. The presence of a time-reversal-breaking mass breaks particle-hole symmetry in the $n = 0$ Landau level. Specifically, the zero mode energies become

$$E_{0\nu} = -\nu m - \eta. \tag{A9}$$

2. Pseudomagnetic Landau levels

The Dirac Hamiltonian in the presence of a pseudomagnetic field $\vec{\mathcal{A}}$ is given by

$$\mathcal{H}(\vec{q}) = \hbar v_F\Gamma_x(q_x + \mathcal{A}_x\Omega^3) + \hbar v_F\Gamma_y(q_y + \mathcal{A}_y\Omega^3), \tag{A10}$$

and $=\vec{\mathcal{A}}(\vec{r})$ is taken so as to describe a constant pseudomagnetic field. In order to solve it, we first introduce dynamical momenta $\hat{\Pi}_x^\pm$ and $\hat{\Pi}_y^\pm$ for each valley $\nu = \pm$, reflecting the fact the sign of the pseudomagnetic field is opposite for the valleys (recall that $\Omega^3 = \nu^z$). The Hamiltonian for each of the valleys reads

$$\mathcal{H}_\pm(\vec{q}) = \pm v_F\begin{pmatrix} & \hat{\Pi}_x^\pm + i\hat{\Pi}_y^\pm \\ \hat{\Pi}_x^\pm - i\hat{\Pi}_y^\pm & \end{pmatrix}, \tag{A11}$$

and the dynamical momenta obey the commutation relations

$$[\hat{\Pi}_x^\pm, \hat{\Pi}_y^\pm] = \mp i\frac{\hbar^2}{l_B^2}, \tag{A12}$$

which follows from Eq. (A1). The commutation relations can be used to define raising and lowering operators in each valley, in terms of which the Hamiltonian takes the form

$$\mathcal{H}_\pm = \pm\begin{pmatrix} & \sqrt{2}\xi\hat{a}_\pm \\ \sqrt{2}\xi\hat{a}_\pm^\dagger & \end{pmatrix} \tag{A13}$$

(with $\xi^2 = v_F^2\hbar^2/l_b^2$) and the operators obey the commutation relation $[\hat{a}_\pm, \hat{a}_\pm^\dagger] = \pm 1$. This commutation relation is a key feature of time-reversal-invariant pseudomagnetic fields, since it reflects antiparallel field alignment in the two valleys. The operation of raising and lowering is interchanged for the two valleys, which has important consequences for the structure of the eigenstates. In particular, the eigenstates of the PLL zero modes are localized on the *same* sublattice, instead of on opposite sublattices. More specifically one has

$$|\Psi_0^+\rangle = \begin{pmatrix} 0 \\ |\varphi_{0,k}\rangle \end{pmatrix}, \quad |\Psi_0^-\rangle = \begin{pmatrix} |\varphi_{0,k}^*\rangle \\ 0 \end{pmatrix}. \tag{A14}$$

We stress that this implies localization on the same sublattice, given the interchange of A and B sublattices in the K_- valley. The $n = 0$ PLL has energy $E = 0$. Eigenstates corresponding to $n \neq 0$ PLLs take the form

$$|\Psi_{n\pm}^+\rangle = \frac{1}{\sqrt{2}}\begin{pmatrix} |\varphi_{n-1,k}\rangle \\ \pm|\varphi_{n,k}\rangle \end{pmatrix}, \quad |\Psi_{n\pm}^-\rangle = \frac{1}{\sqrt{2}}\begin{pmatrix} |\varphi_{n,k}^*\rangle \\ \mp|\varphi_{n-1,k}^*\rangle \end{pmatrix}, \tag{A15}$$

and they have energies $E_\pm(n) = \pm\sqrt{2\xi^2 n}$ for each valley.

APPENDIX B: SETUP OF HARTREE-FOCK CALCULATIONS

Our Hartree-Fock calculations in the presence of the strain superlattice and with interacting Hamiltonian (15) follow the scheme of Ref. [38]. In particular, we choose the unit cell of the unstrained lattice such that it contains six honeycomb lattice sites, as shown in Fig. 6 of the main text. This allows intra-sublattice mean-field structures to form, corresponding to modulation vectors $K_\pm$, which connect the Dirac points of the honeycomb lattice. In terms of the elementary graphene lattice vectors

$$\vec{a}_1 = a(1,\sqrt{2})/2, \quad \vec{a}_2 = a(1,-\sqrt{2})/2,$$

the lattice vectors of the six-site unit cell are given by

$$\vec{b}_1 = 2\vec{a}_1 + \vec{a}_2, \quad \vec{b}_2 = \vec{a}_1 - \vec{a}_2.$$

They are shown in Fig. 6, together with the folded BZ. Figure 6 also shows how, in the presence of the periodic strain superlattice, the superlattice unit cell is defined. The superlattice vectors are $\vec{b}_1$ and $\lambda\vec{b}_2/3$, in terms of the superlattice wavelength λ.

The electronic Hamiltonian is expressed in terms of the fermion annihilation (and corresponding creation) operators

$\hat{\psi}_{\alpha i}(l,\vec{x})$. Here α labels the sublattice (A/B), $i = 1,2,3$ labels the three sites of each sublattice species in the six-site unit cell and $l = 1,\ldots,\lambda$ labels the (six-site) unit cells in the superlattice unit cell, and $\vec{x}$ is a position index for the superlattice unit cell. The Fourier transform is defined as

$$\hat{\psi}_{\alpha i}(l,\vec{k}) = \frac{1}{\sqrt{N}} \sum_{\vec{x}} \hat{\psi}_{\alpha i}(l,\vec{x}) e^{-i\vec{x}\cdot\vec{k}}.$$

The interacting Hamiltonian of Eq. (15) consists of two terms: the NN interaction and the NNN interaction. In momentum space the NN interaction $\hat{H}_{V_1}$ is given by

$$\hat{H}_{V_1} = \frac{V_1}{N} \sum_{\vec{k}\vec{k}'\vec{q}} \hat{\psi}^{\dagger}_{Ai}(l,\vec{k}) \hat{\psi}_{Ai}(l,\vec{k}-\vec{q}) \mathcal{X}_{il,jl'}(\vec{q}) \times \hat{\psi}^{\dagger}_{Bj}(l',\vec{k}') \hat{\psi}_{Bj}(l',\vec{k}'+\vec{q}), \tag{B1}$$

where repeated indices are summed. The matrix function $\mathcal{X}(\vec{q})$ connects NNs, and it is convenient to decompose it in the following way:

$$\mathcal{X}_{il,jl'}(\vec{q}) = \mathcal{X}^{-}_{ij}(\vec{q})\delta_{l,l'-1} + \mathcal{X}^{0}_{ij}(\vec{q})\delta_{l,l'} + \mathcal{X}^{+}_{ij}(\vec{q})\delta_{l,l'+1}.$$

Clearly, $\mathcal{X}^{0}_{ij}(\vec{q})$ connects sites within the same (six-site) unit cell, and it is explicitly given by

$$\mathcal{X}^{0}_{ij}(\vec{q}) = \begin{pmatrix} 1 & 0 & 1 \\ 1 & 1 & 0 \\ e^{i\vec{b}_1\cdot\vec{q}} & 1 & 1 \end{pmatrix}. \tag{B2}$$

The functions $\mathcal{X}^{\pm}_{ij}(\vec{q})$ connect sites in different (six-site) unit cells and each only has a single nonzero entry. They are given by $\mathcal{X}^{+}_{12}(\vec{q}) = e^{-i(\vec{b}_1+\vec{b}_2)\cdot\vec{q}}$ and $\mathcal{X}^{-}_{23}(\vec{q}) = e^{i\vec{b}_2\cdot\vec{q}}$.

Similarly, the NNN interaction Hamiltonian is given by

$$\hat{H}_{V_2} = \frac{V_2}{2N} \sum_{\vec{k}\vec{k}'\vec{q}} \hat{\psi}^{\dagger}_{\alpha i}(l,\vec{k}) \hat{\psi}_{\alpha i}(l,\vec{k}-\vec{q}) \mathcal{Y}^{\alpha}_{il,jl'}(\vec{q}) \times \hat{\psi}^{\dagger}_{\alpha j}(l',\vec{k}') \hat{\psi}_{\alpha j}(l',\vec{k}'+\vec{q}). \tag{B3}$$

The functions $\mathcal{Y}^{\alpha}(\vec{q})$ connect NNNs on each sublattice α. They are directly obtained from Ref. [38], taking into account the additional superlattice index l [in the same way as for $\mathcal{X}(\vec{q})$].

The quartic interactions of the interacting Hamiltonians, schematically written as $\hat{\psi}^{\dagger}_i \hat{\psi}_i \hat{\psi}^{\dagger}_j \hat{\psi}_j$, are decoupled in the standard mean-field way as (written schematically)

$$\rightarrow \hat{\psi}^{\dagger}_i \hat{\psi}_i \langle \hat{\psi}^{\dagger}_j \hat{\psi}_j \rangle + \langle \hat{\psi}^{\dagger}_i \hat{\psi}_i \rangle \hat{\psi}^{\dagger}_j \hat{\psi}_j - \langle \hat{\psi}^{\dagger}_i \hat{\psi}_i \rangle \langle \hat{\psi}^{\dagger}_j \hat{\psi}_j \rangle,$$

$$\rightarrow -\hat{\psi}^{\dagger}_i \hat{\psi}_j \langle \hat{\psi}^{\dagger}_j \hat{\psi}_i \rangle - \langle \hat{\psi}^{\dagger}_i \hat{\psi}_j \rangle \hat{\psi}^{\dagger}_j \hat{\psi}_i + \langle \hat{\psi}^{\dagger}_i \hat{\psi}_j \rangle \langle \hat{\psi}^{\dagger}_j \hat{\psi}_j \rangle,$$

the first line representing charge density order and the second bond density order.

In terms of the actual superlattice electrons, the charge density order parameter is defined as

$$\rho_{\alpha i}(l) = \frac{1}{N} \sum_{\vec{k}} \langle \hat{\psi}^{\dagger}_{\alpha i}(l,\vec{k}) \hat{\psi}_{\alpha i}(l,\vec{k}) \rangle. \tag{B4}$$

Bond order parameters are defined as straightforward generalizations of Ref. [38]. Of particular interest in our case is the QH order parameter, constructed from NNN bond order and defined by Eqs. (21) and (22). To obtain Eq. (21) we decompose $\mathcal{Y}^{\alpha}_{il,jl'}(\vec{k}-\vec{k}')$, which arises due to the reordering of (B3), as

$$\mathcal{Y}^{\alpha}_{il,jl'}(\vec{k}-\vec{k}') = \sum_{\mu=1}^{3} \mathcal{Q}^{\alpha\mu}_{il,jl'}(\vec{k}) \mathcal{Q}^{\alpha\mu}_{il,jl'}(-\vec{k}'). \tag{B5}$$

The sum over μ follows from the three ways in which NNN sites may be connected. Note that $\mathcal{Q}^{\alpha\mu}_{il,jl'}(-\vec{k}) = \mathcal{Q}^{\alpha\mu *}_{il,jl'}(\vec{k})$. We can now give the NNN bond order parameters used to construct the QH order parameter of Eq. (22). The NNN bond order mean fields are defined by

$$\chi^{\alpha}_{il,jl'} = \frac{1}{N} \sum_{\vec{k}} \mathcal{Q}^{\alpha *}_{il,jl'}(\vec{k}) \langle \hat{\psi}^{\dagger}_{\alpha i}(l,\vec{k}) \hat{\psi}_{\alpha j}(l',\vec{k}) \rangle. \tag{B6}$$

The QH order parameter $\Delta_{\mathrm{QH}}(l)$ is defined so that each unit cell labeled by l is associated with 2×9 NNN bonds.

[1] M. Z. Hasan and C. L. Kane, Rev. Mod. Phys. **82**, 3045 (2010).
[2] X.-L. Qi and S.-C. Zhang, Rev. Mod. Phys. **83**, 1057 (2011).
[3] K. S. Novoselov, A. K. Geim, S. V. Morozov, D. Jiang, Y. Zhang, S. V. Dubonos, I. V. Grigorieva, and A. A. Firsov, Science **306**, 666 (2004).
[4] A. H. Castro Neto, F. Guinea, N. M. R. Peres, K. S. Novoselov, and A. K. Geim, Rev. Mod. Phys. **81**, 109 (2009).
[5] L. Fu, C. L. Kane, and E. J. Mele, Phys. Rev. Lett. **98**, 106803 (2007).
[6] G. W. Semenoff, Phys. Rev. Lett. **53**, 2449 (1984).
[7] F. D. M. Haldane, Phys. Rev. Lett. **61**, 2015 (1988).
[8] T. H. Hsieh, H. Lin, J. Liu, W. Duan, A. Bansil, and L. Fu, Nat. Commun. **3**, 982 (2012).
[9] Y. Tanaka, Z. Ren, T. Sato, K. Nakayama, S. Souma, T. Takahashi, K. Segawa, and Y. Ando, Nat. Phys. **8**, 800 (2012).
[10] P. Dziawa, B. J. Kowalski, K. Dybko, R. Buczko, A. Szczerbakow, M. Szot, E. Łusakowska, T. Balasubramanian, B. M. Wojek, M. H. Berntsen, O. Tjernberg, and T. Story, Nat. Matter. **11**, 1023 (2012).
[11] S.-Y. Xu, C. Liu, N. Alidoust, M. Neupane, D. Qian, I. Belopolski, J. D. Denlinger, Y. J. Wang, H. Lin, L. A. Wray, G. Landolt, B. Slomski, J. H. Dil, A. Marcinkova, E. Morosan, Q. Gibson, R. Sankar, F. C. Chou, R. J. Cava, A. Bansil, and M. Z. Hasan, Nat. Commun. **3**, 1192 (2012).
[12] L. Fu, Phys. Rev. Lett. **106**, 106802 (2011).
[13] Y. Ando and L. Fu, Annu. Rev. Condens. Matter Phys. **6**, 361 (2015).
[14] Y. Okada, M. Serbyn, H. Lin, D. Walkup, W. Zhou, C. Dhital, M. Neupane, S. Xu, Y. Wang, R. Sankar, F. Chou, A. Bansil, M. Z Hasan, S. D. Wilson, L. Fu, and V. Madhavan, Science **341**, 1496 (2013).
[15] I. Zeljkovic, Y. Okada, M. Serbyn, R. Sankar, D. Walkup, W. Zhou, J. Liu, G. Chang, Y. J. Wang, M. Z. Hasan, F. Chou, H. Lin, A. Bansil, L. Fu, and V. Madhavan, Nat. Mater. **14**, 318 (2015).
[16] M. Serbyn and L. Fu, Phys. Rev. B **90**, 035402 (2014).
[17] F. Guinea, M. I. Katsnelson, and A. K. Geim, Nat. Phys. **6**, 30 (2010).

[18] M. A. H. Vozmediano, M. I. Katsnelson, and F. Guinea, Phys. Rep. **496**, 109 (2010).
[19] B. Amorim, A. Cortijo, F. de Juan, A. G. Grushin, F. Guinea, A. Gutiérrez-Rubio, H. Ochoa, V. Parente, R. Roldan, P. San-Jose, J. Schiefele, M. Sturla, and M. A. H. Vozmediano, Phys. Rep. **617**, 1 (2016).
[20] K. K. Gomes, W. Mar, W. Ko, F. Guinea, and H. C. Manoharan, Nature (London) **483**, 306 (2012).
[21] N. Levy, S. A. Burke, K. L. Meaker, M. Panlasigui, A. Zettl, F. Guinea, A. H. Castro Neto, and M. F. Crommie, Science **329**, 544 (2010).
[22] V. P. Gusynin, V. A. Miransky, and I. A. Shovkovy, Phys. Rev. Lett. **73**, 3499 (1994).
[23] I. F. Herbut, Phys. Rev. B **78**, 205433 (2008).
[24] P. Ghaemi, J. Cayssol, D. N. Sheng, and A. Vishwanath, Phys. Rev. Lett. **108**, 266801 (2012).
[25] D. A. Abanin and D. A. Pesin, Phys. Rev. Lett. **109**, 066802 (2012).
[26] B. Roy and I. F. Herbut, Phys. Rev. B **88**, 045425 (2013).
[27] B. Roy and J. D. Sau, Phys. Rev. B **90**, 075427 (2014).
[28] B. Roy, F. F. Assaad, and I. F. Herbut, Phys. Rev. X **4**, 021042 (2014).
[29] F. Guinea, M. I. Katsnelson, and M. A. H. Vozmediano, Phys. Rev. B **77**, 075422 (2008).
[30] E. Tang and L. Fu, Nat. Phys. **10**, 964 (2014).
[31] A. Yu. Sipatov, Funct. Mater. **16**, 374 (2009).
[32] L. S. Palatnik and A. I. Fedorenko, J. Cryst. Growth **52**, 917 (1981).
[33] G. Springholz and K. Wiesauer, Phys. Rev. Lett. **88**, 015507 (2001).
[34] S. Gopalakrishnan, P. Ghaemi, and S. Ryu, Phys. Rev. B **86**, 081403 (2012).
[35] F. de Juan, Phys. Rev. B **87**, 125419 (2013).
[36] J. R. Wallbank, M. Mucha-Kruczynski, and V. I. Falko, Phys. Rev. B **88**, 155415 (2013).
[37] S. Raghu, X.-L. Qi, C. Honerkamp, and S.-C. Zhang, Phys. Rev. Lett. **100**, 156401 (2008).
[38] A. G. Grushin, E. V. Castro, A. Cortijo, F. de Juan, M. A. H. Vozmediano, and B. Valenzuela, Phys. Rev. B **87**, 085136 (2013).
[39] C. Weeks and M. Franz, Phys. Rev. B **81**, 085105 (2010).
[40] M. Daghofer and M. Hohenadler, Phys. Rev. B **89**, 035103 (2014).
[41] N. A. Garcia-Martinez, A. G. Grushin, T. Neupert, B. Valenzuela, and E. V. Castro, Phys. Rev. B **88**, 245123 (2013).
[42] T. Đurić, N. Chancellor, and I. F. Herbut, Phys. Rev. B **89**, 165123 (2014).
[43] J. Motruk, A. G. Grushin, F. de Juan, and F. Pollmann, Phys. Rev. B **92**, 085147 (2015).
[44] S. Capponi and A. M. Läuchli, Phys. Rev. B **92**, 085146 (2015).
[45] F. Zhang, J. Jung, G. A. Fiete, Q. Niu, and A. H. MacDonald, Phys. Rev. Lett. **106**, 156801 (2011).
[46] C. W. J. Beenakker, Rev. Mod. Phys. **80**, 1337 (2008).
[47] C.-Y. Hou, C. D. Chamon, and C. Mudry, Phys. Rev. Lett. **98**, 186809 (2007).
[48] J. Liu, W. Duan, and L. Fu, Phys. Rev. B **88**, 241303 (2013).
[49] C. Fang and L. Fu, Phys. Rev. B **91**, 161105 (2015).
[50] J. L. Manes, Phys. Rev. B **76**, 045430 (2007).
[51] P. Ghaemi, S. Gopalakrishnan, and S. Ryu, Phys. Rev. B **87**, 155422 (2013).
[52] N. B. Kopnin, T. T. Heikkilä, and G. E. Volovik, Phys. Rev. B **83**, 220503 (2011).
[53] B. Uchoa and Y. Barlas, Phys. Rev. Lett. **111**, 046604 (2013).